ORIGINAL RESEARCH ARTICLE

Biocorrosion, Biocompatibility Properties, and Bacterial Attachment of Laser Beam Welded AISI 2205 Duplex Stainless Steel

CEYHUN KÖSE, MERVE GÜNDÜZ, ELIF İLHAN, OĞUZHAN GÜNDÜZ, SALIH DURDU, and SERGIO LOZANO-PEREZ

Limited studies exist on the application of welded duplex stainless steel as a temporary implant material. Various methods have been employed to enhance the biocorrosion resistance and biocompatibility of metallic implant materials. In this study, the effect of welding heat input on the biocorrosion behavior and biocompatibility of AISI 2205 duplex stainless steel joined by laser beam welding was investigated. Microstructure and microtexture characterization analyses were also conducted. Electrochemical tests were performed in a simulated body fluid (SBF) environment to evaluate the biocorrosion properties of the welded samples. The results indicated that increasing the welding heat input improved corrosion resistance. This improvement was attributed to the increased austenite volume fraction, larger grain size, and a higher high-angle grain boundary (HAGB) ratio resulting from the higher heat input. Furthermore, it was observed that increasing the welding heat input decreased the water contact angle of the weld zone. In vitro biocompatibility studies were carried out using the MTT assay with an hFOB cell line. Based on the results obtained on days 7, 14, 21, and 28 of incubation, cell viability remained at acceptable levels across all groups. Metal ion release (Cr, Fe, Ni, Mn, and Mo) into the hFOB medium was analyzed using inductively coupled plasma mass spectrometry (ICP-MS), and the results showed that higher heat input reduced ion release. Finally, bacterial adhesion tests performed with *Escherichia coli* revealed that the welding process influenced bacterial attachment. Specifically, higher heat input promoted bacterial adhesion, which was likely associated with the increased surface roughness.

The Handling Editor for this article was Matthias Militzer and the Handling Associate Editor was Krishnan S. Raja.

CEYHUN KÖSE is with the Department of Mechanical Engineering, Faculty of Engineering and Architecture, Tokat Gaziosmanpaşa University, 60150 Tokat, Turkey. Contact e-mail: ceyhun.kose@gop.edu.tr, ceyhunia@gmail.com MERVE GÜNDÜZ is with the Department of Mechanical Engineering, Graduate Education Institute, Tokat Gaziosmanpaşa University, Tokat, Turkey. ELİF İLHAN is with the Center for Nanotechnology and Biomaterials Application and Research (NBUAM), Marmara University, Istanbul, Turkey. OĞUZHAN GÜNDÜZ is with the Center for Nanotechnology and Biomaterials Application and Research (NBUAM), Marmara University and also with the Department of Metallurgical and Materials Engineering, Faculty of Technology, Marmara University, Istanbul, Turkey. SALİH DURDU is with the The Department of Industrial Engineering, Engineering Faculty, Giresun University, Giresun, Turkey and also with the The Department of Genetics and Bioengineering, Engineering Faculty, Giresun University, Giresun, Turkey. SERGİO LOZANO-PEREZ is with the Department of Materials, University of Oxford, Parks Road, Oxford OX1 3PH, UK.

Manuscript submitted January 27, 2026; accepted April 29, 2026.
Article published online May 15, 2026

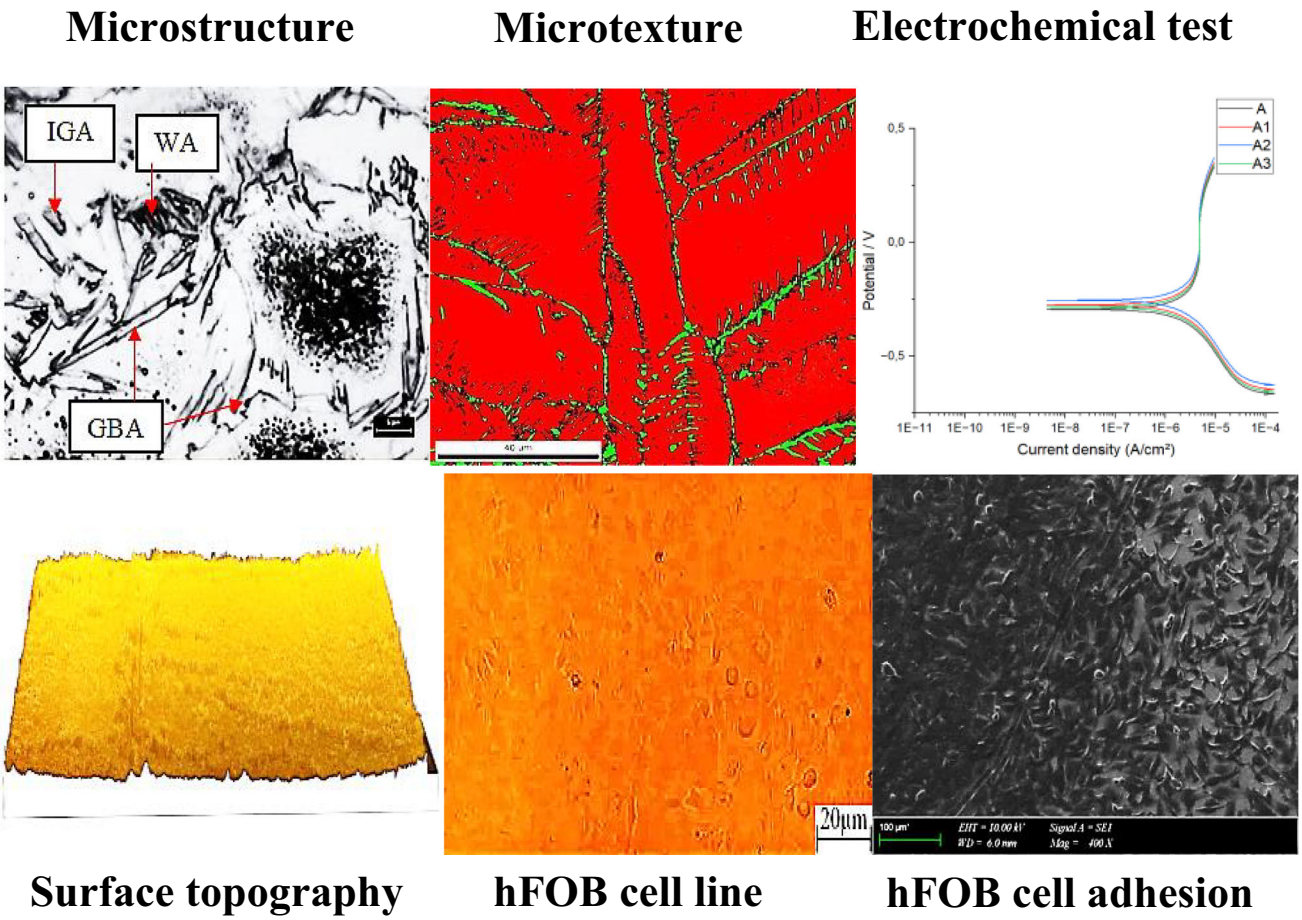

https://doi.org/10.1007/s11661-026-08247-3
© The Author(s) 2026

I. INTRODUCTION

THE most critical requirements for implant materials include optimum mechanical properties, corrosion resistance, biocompatibility, and a surface structure that promotes osseointegration.[1] Currently, austenitic stainless steel is the most preferred metallic material for temporary implants. However, austenitic stainless steels exhibit low corrosion resistance when exposed to aggressive environments containing chloride ions, such as body fluids.[2] Duplex stainless steel (DSS), which demonstrates superior corrosion resistance compared to the 316L austenitic stainless steel used as a metallic implant material, is therefore more advantageous.[3] DSSs are engineering materials that consist of nearly equal proportions of BCC ferrite and FCC austenite crystal structures at room temperature.[4] The balanced ferrite–austenite ratio improves both corrosion resistance and mechanical strength.[4,5] In addition to high corrosion resistance and strength, its soft-magnetic properties enable its use as an implant material.[6–8] Teff *et al.* determined that 2205 DSS can be utilized to produce magnetic stent-grafts owing to its soft-magnetic properties.[6] Furthermore, the elastic modulus and ultimate compressive strength of DSS are significantly higher than those of 316L austenitic stainless steel, making it suitable for bone tissue engineering applications.[8] The corrosion properties of austenitic stainless steels and DSSs, which are considered suitable biomaterials for tissue engineering, have been compared in various studies. *In vitro* and *in vivo* studies, as well as clinical results, suggest that DSS is a viable alternative to biomedical-grade austenitic stainless steel due to its resistance to crevice corrosion in the human body and its superior mechanical properties.[9] Researchers have reported that although 316L austenitic stainless steel is the most commonly used stainless steel in the production of osteosynthesis devices, it may experience localized corrosion issues that can lead to ion release, implant failure, and complications associated with Ni allergy. Therefore, many researchers have stated that DSSs can be used as a replacement for austenitic stainless steels, particularly in bone tissue engineering applications, because of their excellent resistance to localized

corrosion. However, they have cautioned that further research is required due to the limited data available on the magnetic properties of DSSs and their magnetic behavior in biomedical applications. Gregorutti *et al.* investigated the magnetic behavior of DSS alloys and compared the results with austenitic stainless steel. They reported that both materials can be considered soft-magnetic because of the very small area under the hysteresis loop. In addition, the lower Ni content of DSS compared to austenitic stainless steel reduces or minimizes the adverse effects of allergic reactions caused by Ni release. Consequently, DSSs are considered promising alternative materials to austenitic stainless steels for use in the medical industry.[2,8,10]

Metallic implant materials can undergo structural deterioration and corrosion due to exposure to a corrosive environment after being placed in the body.[11] DSS is particularly resistant to stress corrosion and intergranular corrosion.[12] Its high corrosion resistance is directly related to the balanced ferrite–austenite ratio in its structure and the amounts of Cr, Ni, and Mo it contains.[4,13] A high Ni content in the structure promotes an increase in galvanic corrosion resistance by reducing Cr precipitation.[14] Mo participates in the formation of the chromium oxide (Cr_2O_3) passive film in corrosive environments and contributes to increasing the thickness of this film.[15] The addition of Cu increases the localized corrosion resistance of DSS.[16] DSSs exhibit excellent corrosion resistance in various biological environments. In one study, the electrochemical corrosion behavior of 2205 DSS in Ringer's solution was investigated, and the observed corrosion rate supported its suitability as a temporary implant material.[7] In addition, researchers reported that 2205 DSS possesses higher electrochemical corrosion resistance than 316L austenitic stainless steel in simulated physiological Hank's solution and artificial saliva, making its application as an implant material more advantageous.[17,18] DSSs are also utilized in orthodontic wire production owing to their high corrosion resistance.[19]

Numerous approaches have been applied to improve the corrosion resistance and biocompatibility of metallic implant materials.[19–22] Previous researchers have observed that increasing the welding heat input reduces metal ion release from the surface of austenitic stainless steel and improves biocompatibility.[23] In another study, Köse *et al.* concluded that a laser-welded DSS sample kept in L929 fibroblast cell-culture medium exhibited better cell viability than the DSS base material.[24] In the present study, the surface properties, electrochemical corrosion behavior in an SBF environment, and in vitro biocompatibility of 2205 DSS joined using various laser welding heat inputs were investigated. The results obtained from samples joined with different welding heat inputs were compared with those of the base material (BM), thereby systematically evaluating the effects of laser welding heat input on microstructure, microtexture, surface properties, biocorrosion resistance, biocompatibility, and bacterial adhesion. The welding process has a significant impact on the surface properties of stainless steels. In this study, the effects of laser welding heat input on surface topography, wettability, and surface free energy were comparatively examined. Various approaches exist in the literature regarding the relationship between surface properties and biological interactions. This study aims to contribute to the field by explaining the correlation between the biological interactions and surface properties of laser-welded DSS. While various biological electrochemical environments have been used in the literature to investigate the electrochemical corrosion behavior of DSS,[7,17,18] studies determining the electrochemical corrosion behavior of laser-welded DSS in SBF medium remain limited. Furthermore, in vitro biocompatibility analyses of laser-welded DSS reported in the literature are predominantly limited to the L929 fibroblast cell line medium.[24] In this study, the hFOB cell line was utilized for in vitro biocompatibility analyses. The use of the hFOB cell line is crucial for evaluating the biocompatibility of the samples within a human cell line environment and assessing their potential as implant materials for bone tissue. In addition to cytotoxicity studies, the concentration of elements released into the cell-culture medium was determined. After 28 days of incubation, the amount of released elements was found to be well below the levels that could induce cytotoxicity. One of the significant problems associated with metallic implant materials is bacterial contamination. As there are limited studies on determining the quantity of bacteria that can adhere to laser-welded DSS surfaces, the amount of *Escherichia coli* that could adhere to the samples was determined. This study examined both the bacterial adhesion capacity on DSS surfaces and the specific effect of laser welding heat input on this process. Based on the results obtained, laser-welded 2205 DSS can be considered a suitable material for temporary implants.

II. MATERIALS AND METHODS

A. *Material and Welding Process*

In this research, AISI 2205 DSS sheets with dimensions of 300 × 90 × 4 mm were used. The chemical composition (wt pct) of AISI 2205 DSS is shown in Table I. The AISI 2205 DSS sheets were welded using a CO_2 laser beam with three different laser welding heat inputs. The selected laser welding parameters and sample codes are listed in Table II. Test samples were cut using wire electrical discharge machining (WEDM) to determine the microstructure and microtexture of the base material (BM) and laser-welded stainless steel samples, as well as their electrochemical corrosion behavior in the SBF environment, bacterial adhesion, and in vitro biocompatibility (Figure 1). The weld heat input values were calculated using Eq. [1].

$$\text{Heat input (kJ/mm)} = \frac{\text{Laser power (kJ/s)}}{\text{Welding speed (mm/s)}}. \quad [1]$$

Table I. Chemical Composition of AISI 2205 DSS

Element	C	Si	Mn	P	S	Cr	Mo	Ni	Al	Co
Pct	0.028	0.333	1.814	0.011	0.0072	22.88	3.105	5.450	0.019	0.119

Cu	Nb	Ti	V	W	Pb	Sn	Zn	N	Fe
0.224	0.036	0.0089	0.116	0.050	0.0038	0.012	0.034	0.058	65.68

Table II. Sample Codes and Laser Welding Parameters

Samples' Code	Laser Power (W)	Welding Speed (mm/s)	Shielding Gas	Gas Flow Rate (L/min)	Focal Length (mm)	Heat Input (kJ/mm)
A1	3250	30	50 pct Ar + 50 pct He	12	200	0.108
A2	3250	45	50 pct Ar + 50 pct He	12	200	0.072
A3	3750	30	50 pct Ar + 50 pct He	12	200	0.125

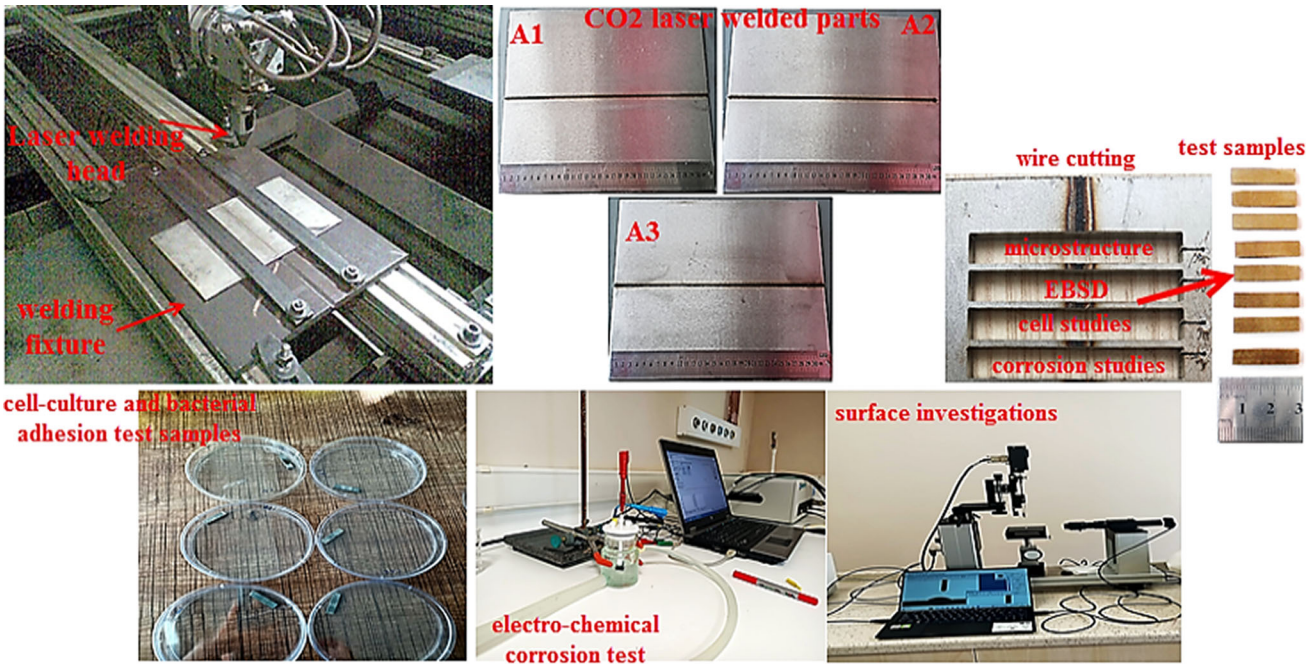

Fig. 1—The weld joint configuration design, schematic drawing of the weld geometry, and a schematic diagram showing the sampling locations and specimen orientations for EBSD, corrosion, and cell-culture assays.

B. *Microstructure and Crystallographic Texture Observations*

To characterize the microstructural changes in the laser-welded samples in detail, the surfaces of the base material and laser-welded samples were polished using sandpaper up to 2000 grit and a velvet polishing cloth, and then etched with Carpenter solution (122 mL C_2H_5OH + 122 mL HCl + 6 mL HNO_3 + 8.5 g $FeCl_3$ + 2.4 g $CuCl_2$). Before the electrochemical corrosion test, in vitro biocompatibility analysis, and bacterial attachment test, the surfaces of the BM and laser-welded samples were polished using sandpaper up to 2000 grit and a velvet polishing cloth. Microstructural examinations of the BM and laser-welded samples were performed using an Olympus optical microscope and a JEOL scanning electron microscope (SEM) and Oxford X-MAX 80 energy dispersive spectroscopy (EDS) connected to the SEM instrument. Crystallographic texture examinations were conducted using a Sigma-Carl Zeiss FEG-SEM equipped with an Oxford Nordlys Nano EBSD detector. Electron Backscatter Diffraction (EBSD) measurement settings were optimized at an acceleration voltage of 20 keV, a working distance of 10 mm, a 120 μm aperture, a 70 deg tilt angle, and step sizes of 0.05 and 0.2 μm. Seven Kikuchi bands were used for indexing each pattern. EBSD maps were obtained using Channel 5 software (Oxford Instruments). XRD

analysis was conducted using a Rigaku device with a scanning speed of 4 deg/min.

C. *Surface Wettability and Surface Free Energy (SFE)*

Contact angle measurements were performed by a sessile drop technique contact angle goniometer (Dataphysics OCA 15EC). The average contact angles were measured within 60 seconds using after 1 μL of deionized water was dropped onto the surfaces. The Neumann technique is predicated on the hypothesis that there is a correlation between the surface free energy (SFE) of a solid (γ_S), the SFE of a liquid in contact with the solid surface (γ_L), and the SFE of the solid–liquid interface (γ_{SL}). This correlation can be described in a general form by the subsequent condition equation [2]:

$$F(\gamma_S, \gamma_L, \gamma_{SL}) = 0. \quad [2]$$

The SFE calculations were conducted by the measurements of the average contact angle (ACA) values for deionized water. Subsequently, the Neumann technique was employed to ascertain the surface energy (γ_S) in accordance with the equation of state. The final form of the equation is shown below[1]:

$$\cos\theta + 1 = 2\left(\frac{\gamma_S}{\gamma_L}\right)e^{[-\beta(\gamma_L-\gamma_S)]}, \quad [3]$$

where $\beta = 0.0001247$ $(m^2/mJ)^2$, $\gamma_L = 72.8$ mJ/m^2, and θ (contact angle) are known for each sample; numerical iteration was needed to solve the Neumann equation.

D. *Surface Topography*

The surface roughness of the samples was determined using a profilometer (surface profiler, KLA Tencor P-7, Milpitas, CA, USA). Surface roughness values were obtained by scanning over a 250 μm $\times$ 250 μm area with 3D mechanical contact and at a speed of 100 μm/s.

E. *Investigation of Electrochemical Corrosion Behavior in SBF Environment*

Before the electrochemical tests, the surfaces of the BM and laser-welded specimens were cleaned by sanitizing in 70 pct ethanol for 1 hour. After surface cleaning, the specimens were dried in an oven (Memmert, Germany) at 50 °C. For the electrochemical corrosion test, an SBF solution prepared according to the recipe of Kokubo and Takadama was used.[25] Electrochemical measurements were carried out at 36.5 °C using a potentiostat/galvanostat (Metrohm Autolab PGSTAT101). Electrochemical measurements were performed using a conventional three-electrode cell consisting of a platinum counter electrode and an Ag/AgCl (3 M KCl) reference electrode. The electrolyte solution was naturally aerated. Prior to polarization tests, the samples were stabilized at open circuit potential for 30 minutes. The Tafel extrapolation technique was used to evaluate the corrosion resistance. Prior to the corrosion tests, the open circuit potential (OCP) of each sample was measured to determine the potential range. Tafel polarization curves were obtained at potentials between − 500 mV below and + 500 mV above the OCP values, with a scan rate of 1 mV/s.

F. *In Vitro Biocompatibility Analysis*

The cytotoxicity of the BM and laser-welded samples was assessed using the extract method, as outlined in ISO 10993-5.[26] The samples were sterilized by using 70 pct ethyl alcohol for 60 minutes and then by holding them under UV light. The sterilized samples were prepared according to ISO-10993-12 standards[27] and added to a complete culture medium [Dulbecco's Modified Eagle's Medium-F12 (DMEM-F12)] supplemented with 10 pct fetal bovine serum (FBS, Gibco) and 1 pct penicillin/streptomycin (Gibco). The samples were kept in the culture medium for 7, 14, 21, and 28 days, and their extracts were separated. Meanwhile, human fetal osteoblastic (hFOB, ATCC-CRL-3602) cell lines were grown in a 5 pct CO_2 incubator (ThermoFisher) at 37 °C using DMEM-F12. Trypsin/EDTA (Gibco) was used to remove the flask when it reached an 80 pct fill rate. Then, the harvested cells were centrifuged at 2000 rpm for 5 minutes, and an appropriate volume of DMEM-F12 was used to lyse the resulting cell pellet. The total number of cells was determined using a cell counter (Anvajo Science). The hFOB cell line was seeded in 96-well plates at 5×10^3 per well and kept in a 5 pct CO_2 incubator (ThermoFisher). After 24 hours of incubation, the medium was separated from the healthy cells, and the previously prepared extracts were added. Negative and positive controls were described by replacing the medium with new culture medium or with 10 pct dimethyl sulfoxide (DMSO). Cells treated with extracts obtained on different days were kept in the incubator for 48 hours. Cell proliferation was evaluated using MTT (3-(4.5-dimethylthiazol-2-yl)-2.5-diphenyltetrazolium Bromide) assay (ElabScience). After adding the extract, MTT solution was added to the specimens and incubated in the incubator for 3 hours. The MTT assay measures the metabolic activity of living cells, while mitochondrial dehydrogenases within the cell reduce MTT and convert it into purple formazan crystals. After incubation, DMSO was added to the wells to form formazan crystals, and the absorbance of the resulting formazan product was calculated at 570 nm using a microplate reader (Agilent BioTek, Epoch). The specimens were performed in triplicate to ensure reproducibility and statistical significance. The absorbance was directly proportional to the number of viable cells. The portion of viable cells was calculated by comparing all specimens and controls with the negative control using the subsequent Eq. [4]:

$$\%\text{Viability} = 100 \times \frac{\text{ODe}}{\text{ODc}}, \quad [4]$$

where ODe shows the average optical density measured for the samples, while ODc defines the mean optical density measured for the negative control, a specimen is

categorized as cytotoxic if the percentage of viability is less than 70 pct, and non-cytotoxic if the percentage of viability is greater than 70 pct.[28]

The amount of elements transferred from the BM and laser-welded samples, joined with different heat inputs into the hFOB cell line medium, was determined. To examine the amount of elements transferred, samples were incubated in the hFOB cell line medium as described above. Inductively coupled plasma mass spectrometry (Thermo Scientific iCAP Q, Italy) was used to determine the elements in the media obtained on the 14th and 28th days of incubation, and the results were read in triplicate. Inductively coupled plasma mass spectrometry (ICP-MS) analyses were carried out using an AGILENT 7700 ICP-MS system equipped with an ASX-500 autosampler. ICP-MS analyses were performed following standard procedures. Samples were digested using appropriate acid mixtures, diluted, and filtered when necessary. Calibration standards were prepared at known concentrations, and an internal standard was used to correct for instrumental drift and matrix effects. Measurements were carried out under optimized argon-plasma operating conditions.

G. *Cell Attachment Analysis*

The BM and laser-welded samples were sterilized by using 70 pct ethyl alcohol for 60 minutes and then by holding them under UV light. The sterilized samples were placed in a 6-well plate and cleaned with Phosphate-Buffered Saline (PBS). Then, the previously propagated hFOB cell line was seeded on the surface of the samples at 20×10^3 cells per well. The cells were incubated with the cells for 48 hours. After the culture media were removed, the samples were cleaned with 0.1 M cacodylate buffer (ThermoScientific) (pH 7.4), and the cells were fixed by adding 2.5 pct glutaraldehyde to the sample surface for 20 minutes. Post-fixation, the specimens were cleaned with cacodylate buffer and dried. After the specimens' surface was coated with gold and palladium for 60 seconds with the help of a sputter coating machine (Quorum SC7620, USA), cell morphologies were analyzed by SEM (Zeiss EVO LS 10).

H. *Bacterial Adhesion Test*

Escherichia coli O157:H7 ATCC 25922 was used as the test culture for the bacterial adhesion assay. The test culture was activated by incubating in Brain Heart Infusion Broth (BHIB, Condalab, 201181, Spain) at 37 °C for 24 hours. The method applied by Zhai *et al.* was modified for the bacterial adhesion test of the samples.[29] Before the experiment, the specimens were sterilized by autoclaving. Sterile specimens were immersed in the bacterial suspension adjusted to 106 CFU/mL and incubated at 37 °C for 24 hours. At the end of the incubation period, the samples were washed with 20 mL of peptone water to remove bacteria that did not attach to the surface. After washing, the samples were transferred to tubes containing 10 mL of peptone water, and vortexing was performed for 3 minutes to separate bacteria adhering to the surface. Using the spread plate method, decimal dilutions were prepared from the resulting culture suspension and inoculated onto Brain Heart Infusion agar (BHIA, Condalab, 112141). Bacteria adhering to the surface were evaluated by colony counting, and the values obtained were expressed as colony-forming units (log cfu/mL cm^2).

The adhesion of *E. coli* O157:H7 to the surface of BM and laser-welded AISI 2205 DSS samples under different welding heat inputs was visualized by SEM. The method used by Klug *et al.* was applied with a modification.[30] The samples were incubated as mentioned above and then washed. They were then fixed in 10 mL of 2.5 pct glutaraldehyde solution for 24 hours. Following fixation, the samples were cleaned with 10 mL of peptone water and then dehydrated by soaking in ethanol at concentrations of 50, 60, 70, 80, and 90 pct for 10 minutes. The samples were then immersed first in 50 pct ethanol, then in 50 pct acetone, and then held in pure acetone for 10 minutes. The specimens were dried in a biosafety cabinet for 12 hours after this process. Bacterial adherence was visualized using SEM.

I. *Statistical Analysis*

Biological and chemical analyses were designed with three replicates. The bacterial adhesion and ICP-MS data were analyzed using the SPSS (IBM SPSS Statistics 26.0) statistical package program, initially using ANOVA, followed by Duncan's test for group comparisons. Cell viability data were evaluated using pairwise two-tailed Student's *t*-tests.

III. RESULTS AND DISCUSSION

A. *Microstructure and Crystallographic Texture Observations*

Optical microscope (OM) and SEM images of AISI 2205 DSS are indicated in Figure 2. In the microstructure images, light-colored structures indicate austenite grains, while dark-colored structures indicate ferrite grains (Figure 2).

From OM and SEM images, greater austenite formation was observed in the weld metal of sample A3, which was joined with a high welding heat input, compared with sample A2, which was joined with a low welding heat input (Figure 3). Due to rapid solidification associated with low welding heat input, the weld microstructure consisted of coarser ferrite grains, and the ferrite–austenite balance shifted in favor of ferrite as the ferrite grains coarsened (Figure 3). Furthermore, undesirable phases such as sigma phase or nitride/carbide precipitates, which reduce mechanical properties (ductility, toughness, and sometimes fatigue resistance) and corrosion resistance, were not observed in the microstructure of the welded joints. Solidification modes in stainless steels are significantly influenced by their chemical composition during cooling from elevated temperatures. The DSS weld microstructure develops in a purely ferritic solidification mode in the following

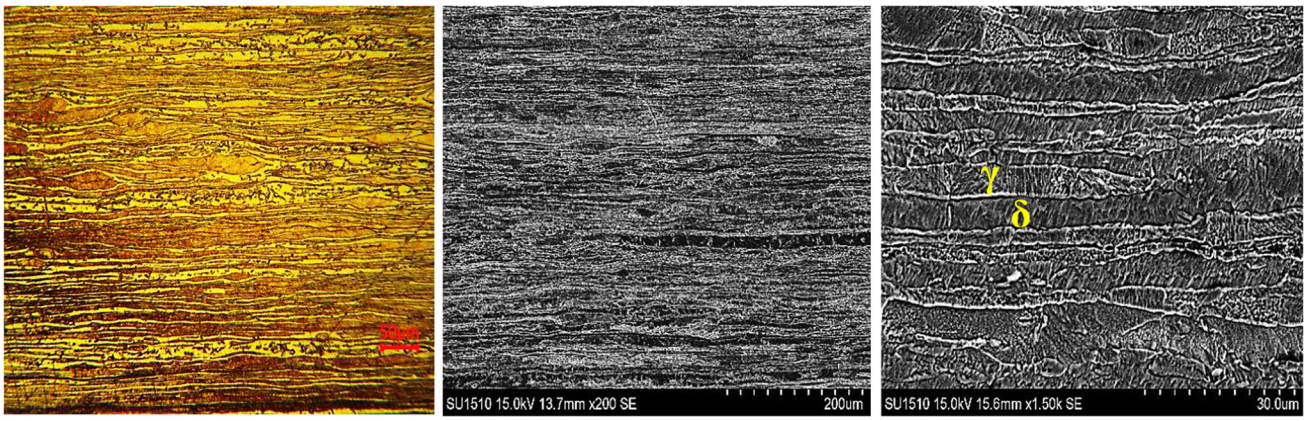

Fig. 2—OM and SEM Secondary Electron (SE) images of the BM.

sequence: liquid → (liquid + ferrite) → ferrite → (ferrite + austenite). The DSS weld metal solidifies entirely as ferrite, and the austenite volume fraction develops through solid-state phase transformation.[32] The ferrite phase forms from the liquid by primary solidification and persists until solidification is complete. The transformation of austenite from the ferrite phase occurs later through a solid-state transformation, namely the diffusion-controlled $\delta \rightarrow \gamma$ transformation, and more austenite generally forms under slow cooling conditions. Primary austenite phase formation occurs during the welding process, followed by grain growth within the ferrite. During the cooling of the weld metal, the ferrite phase partially transforms into the austenite phase. The cooling rate plays a significant role in phase formation in DSSs.[33] High heat input during welding reduces the cooling rate and promotes the formation of austenitic phases.[34] Laser welding is a highly efficient joining method with minimal impact on the workpiece and the heat-affected zone (HAZ). The low welding heat input and high cooling rate associated with laser welding contribute to the formation of fine grains in the weld metal.[35] It is known that DSSs joined by laser welding maintain their duplex structure; however, samples joined with high welding heat input generally exhibit higher austenite content.[36] During the cooling of the weld pool, various morphologies develop in the HAZ.[37] The first type of nucleation is defined as grain boundary austenite (GBA) and occurs along the δ/δ grain boundaries.[13,32] In addition, Widmanstätten austenite (WA) is likely to form from GBA within the ferrite grains.[32] It grows rapidly from the GBA boundary toward the ferrite grains as side plates, forming WA.[38] The third type of austenite, intragranular austenite (IGA), can precipitate within ferrite grains during cooling. In the case of slow cooling, the formation of intragranular austenite (IGA) occurs more readily.[37] The formation of IGA requires a greater degree of undercooling (as the driving force) compared to GBA and WA owing to the higher activation energy required for lattice diffusion. Compared with lattice diffusion, grain boundary diffusion occurs relatively faster; consequently, IGA growth is generally more limited than that of GBA and WA.[31] As a result of joining DSSs using laser welding, a microstructure consisting of GBA, IGA, and WA can form.[35,39–41] In this study, consistent with the literature, the weld microstructure of DSSs joined with various welding heat inputs was examined, and the formation of GBA, IGA, and WA was observed (Figure 3). An increase in welding heat input not only affects the formation of the austenite phase but also has a significant impact on austenitic morphology.[42]

B. *SEM–EDS and XRD Analysis*

The results of SEM–EDS point analysis and line-scan analysis of the laser-welded samples are presented in Figures 4 and 5. In addition, the quantitative compositional data obtained from EDS point analyses of ferrite and austenite grains in the BM and WM microstructures are shown in Table III.

Line-scan analyses of samples welded with different heat inputs revealed no significant differences in the elemental distribution of Fe, Cr, Ni, and Mo. Only minor fluctuations were observed, indicating a homogeneous elemental distribution (Figure 4). As expected, small fluctuations were detected in the analyses of ferrite and austenite grains due to their different chemical compositions. According to the line-scan analysis results, no significant elemental changes occurred as a result of variations in laser welding heat input, and no elemental changes indicative of undesirable secondary phases or chromium nitride formations were observed. Owing to the inherent characteristics of laser welding processes, which involve low heat input and rapid solidification, the formation of undesirable structures is unlikely, as insufficient time is available for their formation. However, the high power density associated with laser welding processes can sometimes lead to the formation of carbide precipitates within grains or at grain boundaries, particularly due to local reductions in Cr content. In joints produced with high power density (*i.e.*, high heat input), chromium migration toward grain boundaries may occur, and chromium depletion in these regions could increase susceptibility to corrosion. Nitride formations are known to contain higher amounts of Cr, Fe, Mo, and V, whereas Ni and Cu contents are typically lower. The results of EDS point

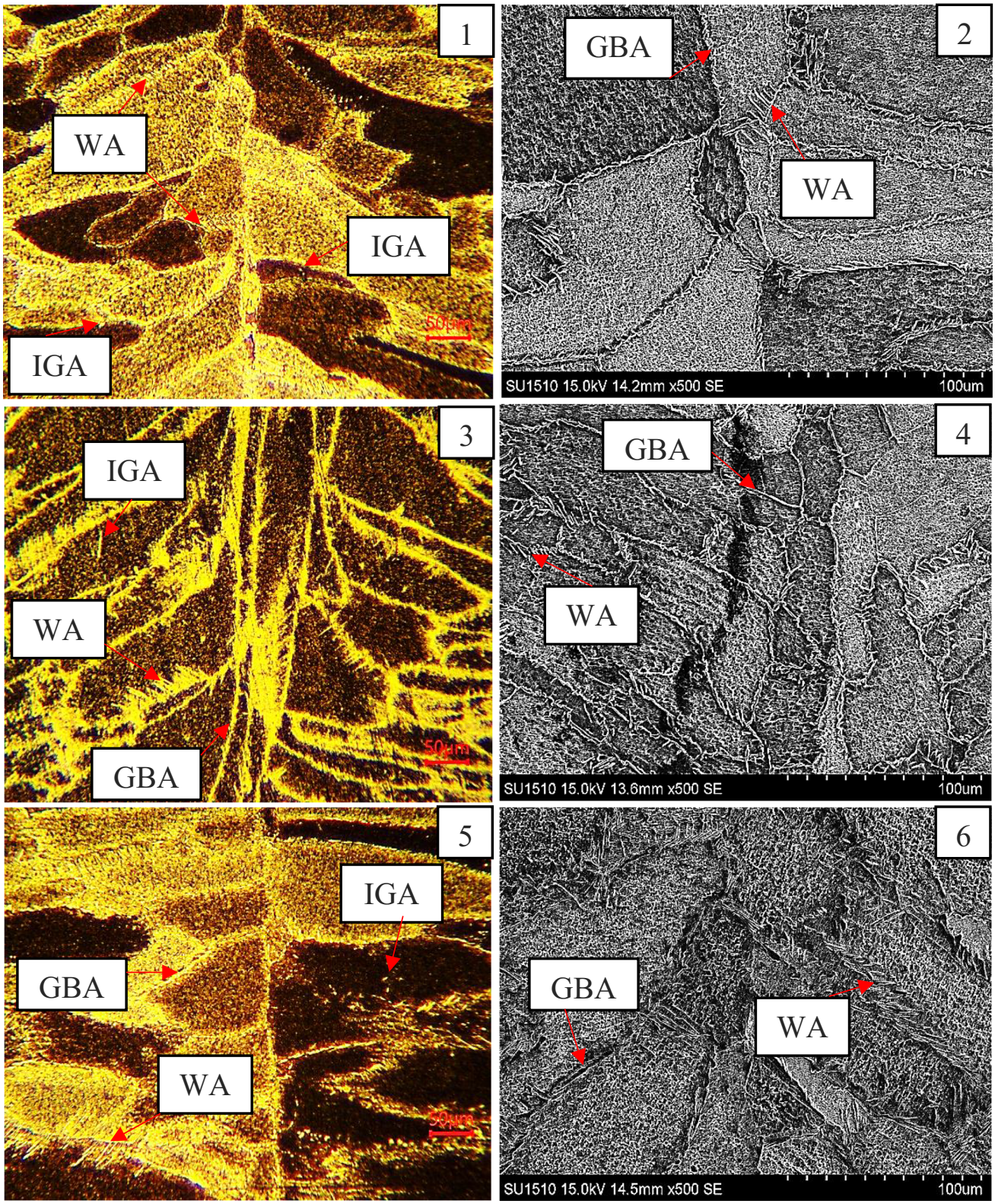

Fig. 3—Optical microscope and SEM SE images of laser-welded samples, 1: OM image of A1, 2: SEM image of A1, 3: OM image of A2, 4: SEM image of A2, 5: OM image of A3, and 6: SEM image of A3.

analyses conducted on austenite and ferrite grains (Figure 5) showed no significant differences either compared with the base material or among the welded joints. Based on the EDS line-scan and EDS point analysis results, the effect of welding heat input was found to be limited in DSS samples joined with different

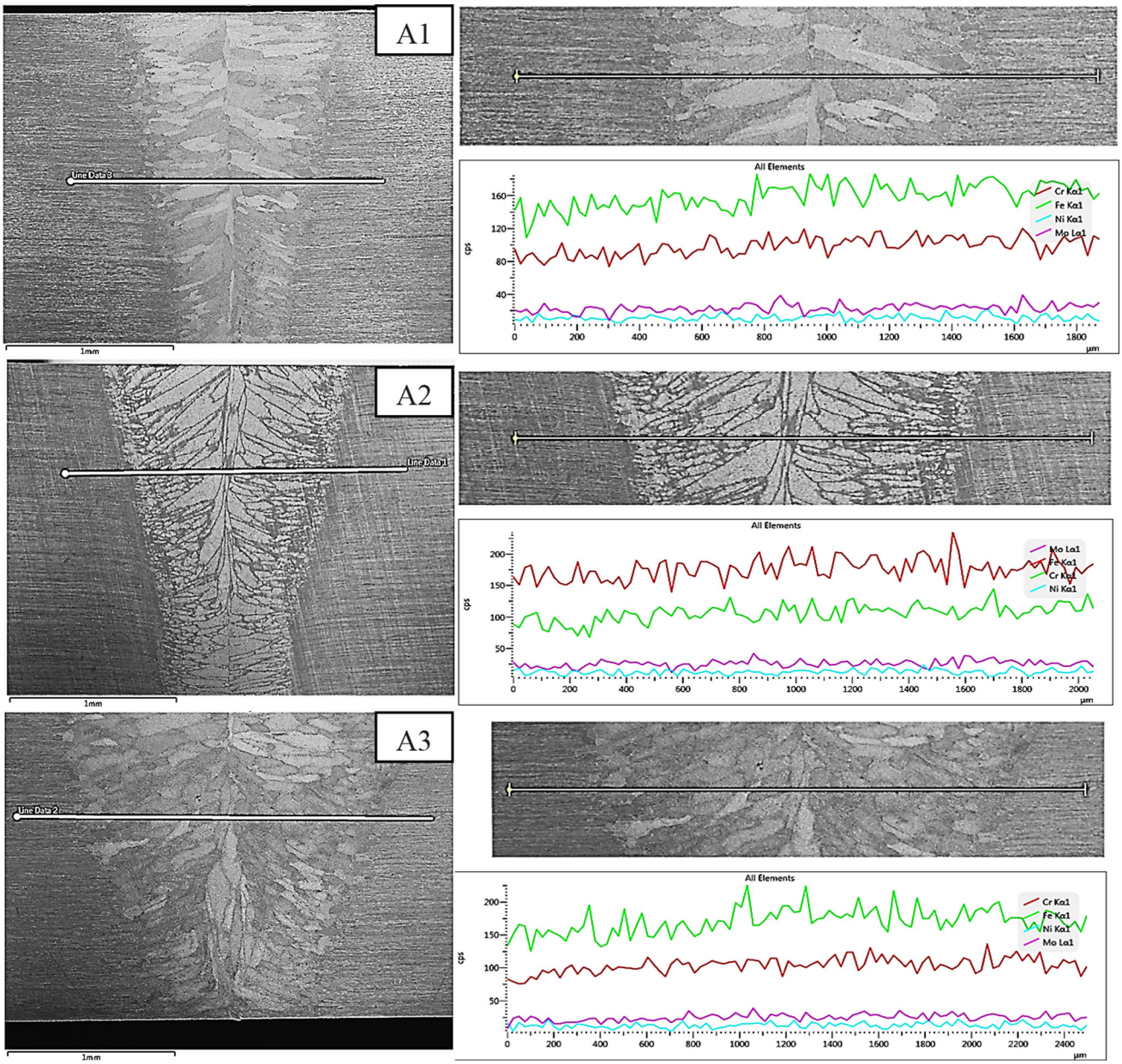

Fig. 4—SEM–EDS line-scan analysis of samples A1, A2, and A3.

welding heat inputs. Because no significant elemental losses were detected, the samples are expected to exhibit high corrosion resistance in aggressive environments.

XRD analyses of the laser-welded samples were conducted, and the resulting diffraction peaks are presented in Figure 6. The effect of welding heat input on the XRD patterns of the laser-welded joints is clearly visible, as the peak intensities change with variations in heat input. δ-Ferrite and γ-austenite phases were detected in samples A1, A2, and A3. No undesirable phases other than ferrite and austenite, such as chromium carbide/nitride precipitates or other secondary phases, were detected.

It should also be noted that such undesirable structures may not be detectable by XRD due to their very low volume fraction in the weld microstructure.

C. *EBSD*

To understand the impact of welding heat input on the grain orientation and texture of the weld microstructure, image quality (IQ) maps, inverse pole figure (IPF) maps, phase maps, grain size maps, grain orientation spread (GOS) maps, rotational grain boundary angle maps, kernel average misorientation (KAM) maps, and pole figure maps were obtained *via* EBSD analysis (Figures 7, 8, and 9). These maps provide information on the orientations and microtexture characteristics of austenite and ferrite grains. The results clearly indicate that epitaxial solidification occurs at the weld center of the laser-welded joints. It was observed that the BM grains exhibited random orientations (Figure 7(b)). The ferrite grains in the weld center of sample A2 were

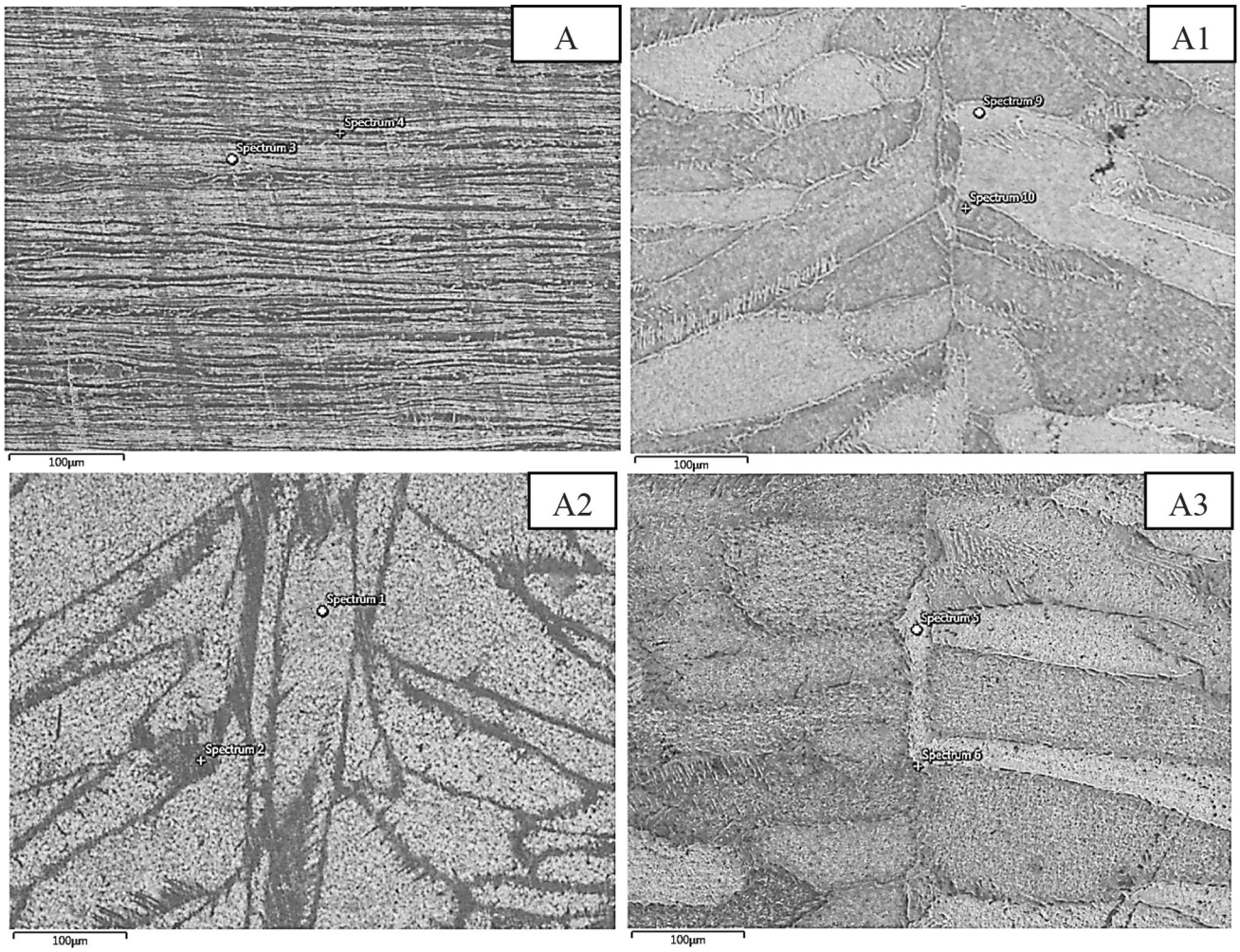

Fig. 5—SEM–EDS point analysis of samples A, A1, A2, and A3.

Table III. EDS Point Analysis Results of BM and WMs (Wt Pct)

Samples	Cr	Ni	Mo	Fe	Phases
A	25.6	4.7	3.6	65.9	δ-ferrite
	24.0	5.6	3.5	66.3	γ-austenite
A1	24.2	5.2	3.4	67.1	δ-ferrite
	24.2	5.8	3.4	66.4	γ-austenite
A2	24.1	4.6	3.8	67.4	δ-ferrite
	25.6	5.2	3.2	65.9	γ-austenite
A3	24.0	5.4	3.4	67.0	δ-ferrite
	24.6	5.1	3.3	66.9	γ-austenite

mainly oriented near the [111] and [001] directions, whereas the austenite grains exhibited a predominantly random orientation (Figure 8(b)). In contrast, the ferrite grains in the weld center of sample A3 were also oriented along the [111] and [001] directions, while the austenite grains were mostly oriented closer to the [001] direction and away from the [101] direction (Figure 9(b)). The presence of random texture is attributed to the relatively weak texture typically

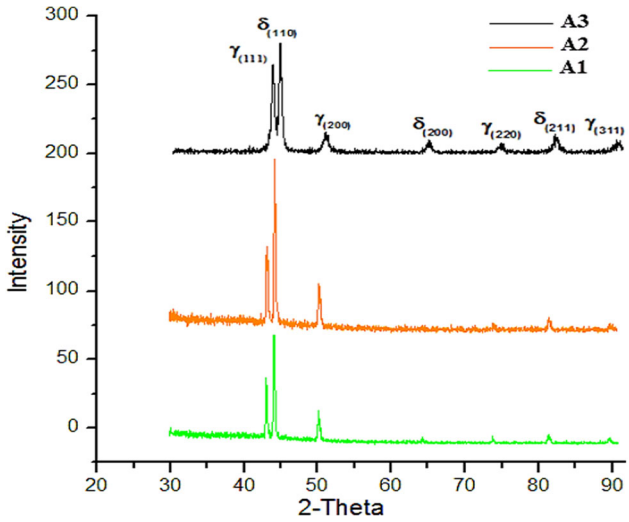

Fig. 6—XRD analysis results.

observed in laser-welded joints.[43] In particular, the columnar grains in the weld center of sample A2 were observed to develop along the direction of heat flow

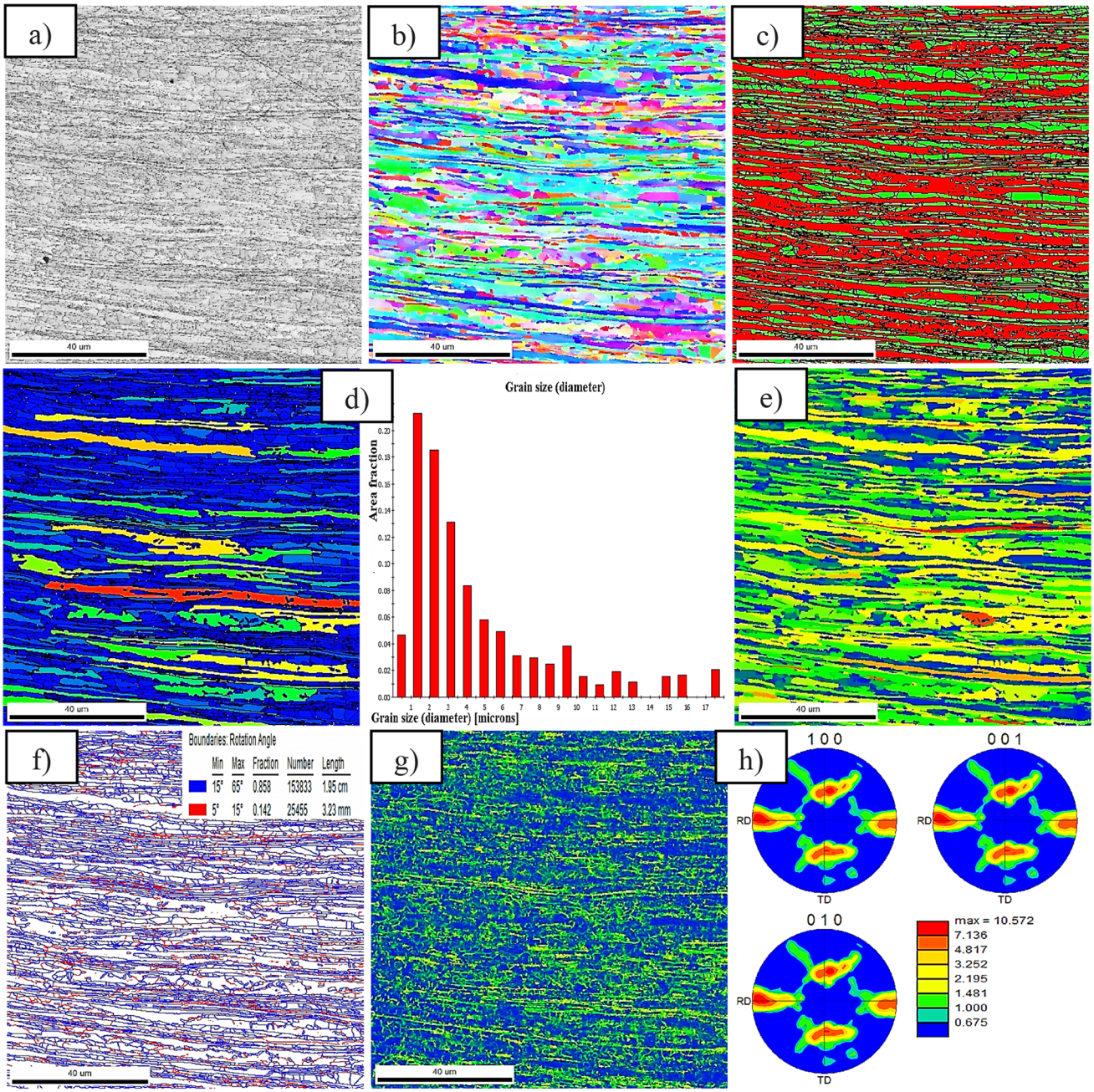

Fig. 7—EBSD analysis results of BM: (*a*) IQ map, (*b*) Inverse pole figure, (*c*) Phase map, (*d*) Grain size, (*e*) GOS, (*f*) Rotational grain boundary angle map, (*g*) KAM, and (*h*) Pole figure for the Ferrite.

(Figure 8). During laser welding, the directions of heat flow and cooling during the solidification of the liquid weld metal are important parameters affecting the resulting texture.[44,45] It is evident that the direction of local heat transfer significantly contributes to the grain orientation in the weld center. When the volume fractions of δ-ferrite and γ-austenite phases in the base material and the weld metal of samples A2 and A3 are examined, the ferrite and austenite ratios of the BM are 53 and 47 pct, respectively, whereas the ferrite and austenite ratios are 90 and 10 pct for sample A2 and 86 and 14 pct for sample A3 (Figures 7(c), 8(c), and 9(c)). Because laser welding involves relatively low welding heat input, rapid solidification occurs in the weld pool, resulting in an increased ferrite volume fraction. It was also observed that the grain sizes in the weld center of samples A2 and A3 were relatively similar, although the grain size in sample A3 was slightly larger due to the higher welding heat input (Figures 8(d) and 9(d)).

GOS maps describe the degree of recrystallization; grain orientation spread (GOS) maps of ferrite and austenite are presented in Figures 7(e), 8(e), and 9(e). Blue and green regions, which correspond to low GOS values, were observed in the weld centers of samples A2 and A3. These low GOS values indicate the presence of subgrains in the weld centers of samples A2 and A3.

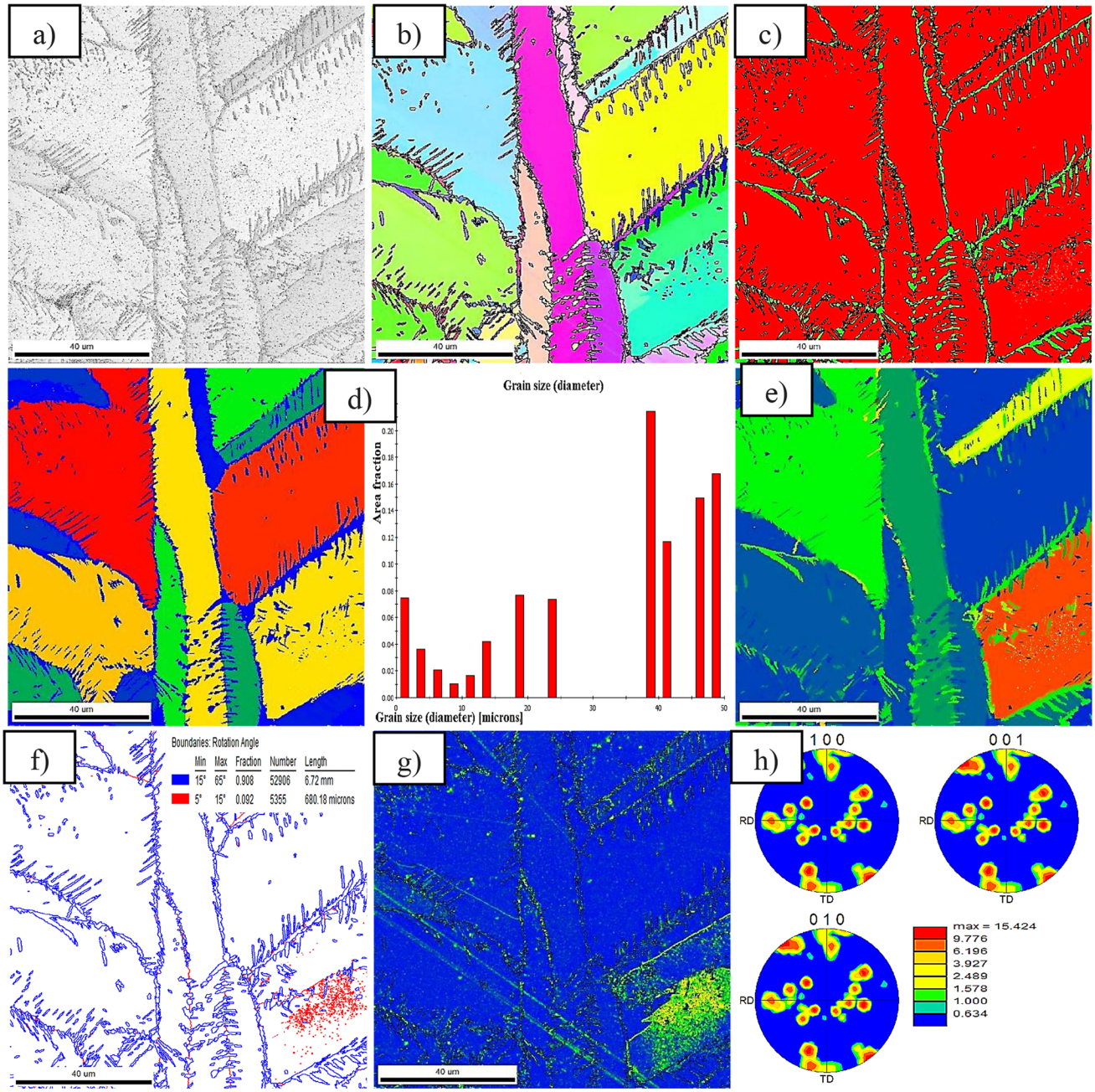

Fig. 8—EBSD analysis results of A2 sample: (*a*) IQ map, (*b*) Inverse pole figure, (*c*) Phase map, (*d*) Grain size, (*e*) GOS, (*f*) Rotational grain boundary angle map, (*g*) KAM, and (*h*) Pole figure for the Ferrite.

Owing to variations in welding heat input, high GOS values were observed in some ferrite and austenite grains in the weld centers of both samples, whereas low GOS values were observed in others. High GOS values (orange and red regions) indicate that the grains are not fully recrystallized, while low GOS values indicate that recrystallization has occurred. GOS also provides a quantitative description of the crystallographic orientation gradients within individual grains. The GOS value was found to be relatively higher in sample A2 than in sample A3. The rotation angle is defined as the angle between two grains in the same phase that are not in direct contact but share a common axis. The misorientation angle is defined as the minimum rotation angle about a common axis that causes two grains in the same phase that are not in direct contact to coincide. It represents the degree of mismatch between the crystal structures of neighboring grains.[46] Grain boundaries (GBs) are generally classified into two groups: low-angle grain boundaries (LAGBs, < 15 deg) and high-angle grain boundaries (HAGBs, > 15 deg). HAGBs can also be categorized as special and random boundaries. GBs with $\Sigma \leq 29$ are defined as special boundaries, whereas GBs with $\Sigma > 29$ or non-coincidence site lattice (CSL) boundaries are defined as random HAGBs.[43,46] HAGBs hinder dislocation motion and improve the

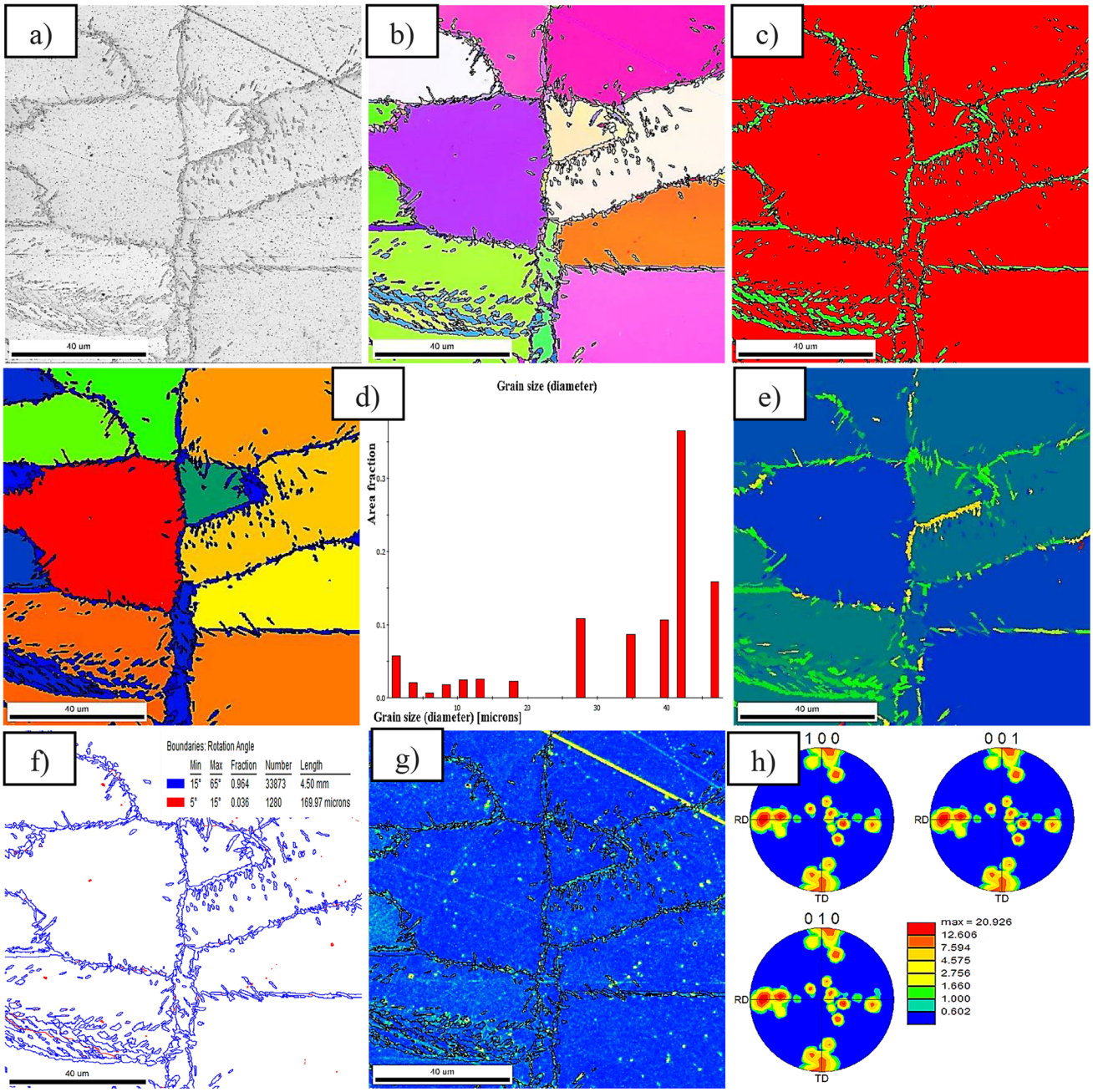

Fig. 9—EBSD analysis results of A3 sample: (*a*) IQ map, (*b*) Inverse pole figure, (*c*) Phase map, (*d*) Grain size, (*e*) GOS, (*f*) Rotational grain boundary angle map, (*g*) KAM, and (*h*) Pole figure for the Ferrite.

tensile strength, yield strength, and hardness of materials.[46] When the GB maps (Figures 7(f), 8(f), and 9(f)) were examined, it was determined that HAGBs with rotation angles greater than 15 deg (fraction of 0.858) were dominant in the BM. In contrast, LAGBs with rotation angles less than 15 deg (fraction of 0.992) were dominant in the weld center of sample A2, whereas HAGBs with rotation angles greater than 15 deg (fraction of 0.954) were dominant in the weld center of sample A3. HAGBs have higher energies due to the increased misorientation between grains. As a result of the influence of laser welding heat input, grain boundary angles changed during recrystallization, particularly under conditions of rapid solidification associated with low heat input.

KAM maps were obtained to identify local grain misorientation in ferrite, austenite, and grain boundaries (GBs), and these maps are presented in Figures 7(g), 8(g), and 9(g). Dislocation formation in a material results from local variations in lattice orientation.[38,43,46] In other words, the KAM distribution reflects the dislocation density distribution within different grains.[38,43,46,47] It was determined that the BM exhibited more complex KAM values. The KAM value, which represents local dislocations, was found to be generally higher within ferrite grains and at their

boundaries than within austenite grains. The KAM maps also revealed local increases in dislocation density at the GBs in the weld centers of samples A2 and A3, particularly within ferrite grains. Although the KAM values were very similar, the KAM value was relatively lower in sample A3 due to the increase in welding heat input. Two main theories describe the relationship between dislocation density and corrosion resistance. The first theory proposes that increased dislocation density is associated with a higher concentration of corrosion-active sites within the material, which can reduce corrosion resistance. In contrast, the second theory suggests that a uniform increase in dislocation density leads to a greater number of corrosion-active sites. This, in turn, provides additional nucleation sites and a stronger driving force for passive film formation. Dislocations also act as fast diffusion paths; therefore, a higher dislocation density alters the diffusion kinetics of oxygen and solute atoms diffusing outward. In many alloys, it has been observed that a more deformed surface (*e.g.*, after shot-peening or coarse grinding) can form a more protective oxide layer.[48] Pole figures were obtained to examine the crystallographic textures of the BM and welded samples, and the results are presented in Figures 7(h), 8(h), and 9(h). Texture densities indicating strong textures at the weld center were determined for the BM (maximum texture intensity of 10.572), A2 (maximum texture intensity of 15.424), and A3 (maximum texture intensity of 20.926) samples. The texture density was particularly pronounced in the ⟨011⟩// welding direction. These texture densities indicate that the samples have a high potential for anisotropic behavior. A preferred crystallographic orientation developed due to the epitaxial growth of columnar grains in the weld center. Previous studies have reported that the duplex (ferrite + austenite) weld microstructure exhibits a stronger texture than a purely austenitic microstructure.[43] This can be explained by the stronger texture density of ferrite grains compared with austenite grains. It should be clearly emphasized that, due to the influence of welding heat input, grain morphology changes significantly, grains undergo recrystallization, and preferred grain orientations develop within the weld microstructure.

D. *Results of Electrochemical Corrosion Test in SBF Environment*

The corrosion behavior of the BM and laser-welded samples was comparatively analyzed using potentiodynamic polarization in the SBF environment. To evaluate the corrosion performance, corrosion potential (E_{corr}), corrosion current density (I_{corr}), corrosion rate, and polarization resistance (R_p) values were determined from the Tafel curves using Nova computer software (Table IV). The potentiodynamic polarization curves of the samples obtained in the SBF environment are presented in Figure 10.

It was determined that the AISI 2205 DSS base material exhibited higher corrosion resistance compared to the welded samples owing to its higher E_{corr} value and lower I_{corr} value. As is known, according to Faraday's law of electrolysis, a rise in E_{corr} and a reduction in I_{corr} result in increased corrosion resistance.[49] Furthermore, it was determined that the BM had the highest polarization resistance among the samples. It was observed that a rise in polarization resistance resulted in increased corrosion resistance. An increase in welding heat input promotes an increase in the austenite content in the structure of DSS. A high rate of austenite phase formation is directly related to an increase in electrochemical corrosion resistance.[33] An increase in welding heat input allows the austenite phase fraction to develop while reducing the formation of structures such as chromium nitride, thus improving corrosion resistance.[50] In this study, the microstructure did not show formations such as sigma phase, carbides, or nitrides that could negatively affect corrosion resistance.

Owing to the fast cooling caused by low welding heat input, laser welding reduces the time required for the formation of undesirable structures such as carbides and nitrides. Furthermore, laser-welded joints require lower welding heat input than other traditional fusion welding methods, resulting in a finely structured morphology in the weld metal. Moreover, the rapid solidification resulting from low welding heat input leads to a narrow weld bead and a narrow heat-affected zone (HAZ). Because a narrow weld bead and HAZ imply a less transformed microstructure in terms of weld metallurgy, this condition is expected to positively affect mechanical properties and corrosion resistance. A fine-grained microstructure results in a larger surface area, which can lead to better corrosion resistance in some aggressive corrosive environments. When the electrochemical corrosion behavior of DSS samples joined with different welding heat inputs in SBF was examined, the lowest corrosion rate was observed in sample A3, which was joined with the highest welding heat input, while the highest corrosion rate was observed in sample A2, which was joined with the lowest welding heat input (Table IV). According to this result, electrochemical tests revealed that laser-welded DSS joined with low heat input had higher corrosion susceptibility. Similar results have been reported by other researchers, namely that DSS samples joined with high welding heat input exhibit higher electrochemical corrosion resistance than samples joined with low welding heat input.[33,42,51–55] The corrosion rates of samples A1 and A2 were determined to be 0.0117 mm/year and 0.0146 mm/year, respectively. Based on these results, it was concluded that increasing the laser welding speed supported an increase in the electrochemical corrosion rate in the SBF environment. Researchers have emphasized that some metallic materials exhibit improved corrosion resistance with microstructural refinement owing to increased passivation capacity. In contrast, others have reported that grain refinement may deteriorate corrosion resistance owing to increased active sites in the form of grain boundaries, GBs.[56] There is no consensus on the impact of grain size on corrosion behavior, as it is challenging to isolate grain size from other processing-induced microstructural changes. In other words, in addition to grain size, microstructural changes such as texture, impurities, and secondary phases can

Table IV. Electrochemical Corrosion Values of BM and Laser-Welded Samples in SBF Environment

Samples	OCP (V)	E_{corr} (V)	I_{corr} (A/cm^2)	Corrosion Rate (mm/year)	Polarization Resistance (Ω)
A	0.170	− 0.2403	6.2739×10^{-7}	0.0072	41534
A1	0.162	− 0.2840	1.0118×10^{-6}	0.0119	25753
A2	0.151	− 0.2640	1.2582×10^{-6}	0.0146	20711
A3	0.134	− 0.2752	1.0046×10^{-6}	0.0110	25938

$n = 1$.

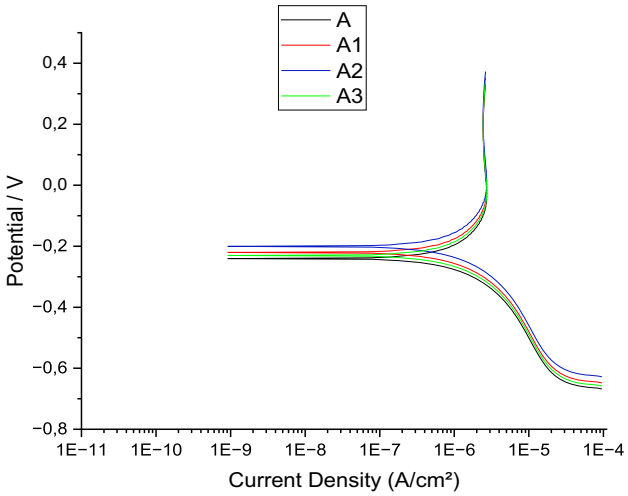

Fig. 10—Potentiodynamic polarization diagram of the BM and laser-welded samples.

significantly affect corrosion behavior. In this study, among the welded samples, the lowest corrosion rate was observed in sample A3, which was joined with the highest welding heat input, while the highest corrosion rate was observed in sample A2, which was joined with the lowest welding heat input. Therefore, according to our results, sample A3, which consists of coarse grains and is dominated by HAGBs with a rotation angle greater than 15 deg (fraction of 0.954) at the weld center, exhibited the best corrosion performance. In contrast, sample A2, which is composed of fine grains and is dominated by LAGBs with a rotation angle of less than 15 deg (fraction of 0.992) at the weld center, exhibited the lowest corrosion performance. It should be clearly emphasized that the results obtained here reveal a more complex relationship between HAGBs/LAGBs and corrosion behavior than initially described and that these should not be interpreted as precise mechanisms. The effect of grain boundary characteristics on corrosion is known to depend on various factors, including segregation, misorientation angle, and the specific environment. Therefore, the trends observed here represent correlations derived from microstructural and microtextural analyses rather than precise mechanistic explanations. The results obtained are correlations that suggest directions for future, more fundamental studies. While the ferrite grains at the weld center of samples A2 and A3 exhibited similar crystallographic orientations (mostly orientations close to the [111] and [001] directions), the austenite grains at the weld center of sample A2 exhibited predominantly random orientations, whereas the austenite grains at the weld center of sample A3 exhibited orientations closer to [001] and away from [101], as determined in the previous section. The high corrosion resistance of the [101] crystallographic plane is attributed to its higher atomic packing density.[56] In addition, the ferrite and austenite ratios of sample A2 were obtained as 90 and 10 pct, respectively, whereas those of sample A3 were obtained as 86 and 14 pct in the previous section. Researchers have reported that acicular ferrite tends to exhibit reduced corrosion resistance owing to the large number of high-energy, wide-angle GBs.[57] Other researchers have suggested that a moderate increase in grain size can facilitate GB growth and structural refinement, which in turn can reduce the incidence and rate of propagation of corrosion processes.[48] The results indicate that the coarsening of the weld microstructure, including GBs, crystallographic orientations, and microstructural transformations, has a substantial effect on the corrosion performance of DSS.

Although the welding process was conducted using the laser welding method, which produces low heat input, it is evident that all samples were affected by the welding thermal cycle and that the weld zone exhibited greater sensitivity than the BM. It can be stated that the amount of thermal energy transferred to the weld zone specifically the variations in welding heat input affects the morphology of the Cr_2O_3 layer formed in the weld zone, and the texture of this layer subsequently influences the corrosion rate. It is clear that the chemical composition and physical properties of the Cr_2O_3 layer, particularly the repassivation formation time, are influenced by changes in welding heat input. Furthermore, the results of the electrochemical corrosion tests indicate that the corrosion rates remained low. The protective Cr_2O_3 layer formed on the surface of the BM and the laser-welded samples supported the stability of the specimens in SBF. The Cr_2O_3 film formed on the surface of stainless steels inhibits the transport of metallic ions in physiological environments, resulting in lower corrosion rates and improved biocompatibility.[23,24,58] A thin passive Cr_2O_3 film develops on the surface of high-chromium stainless steels, covering the surface through the passivation process. DSSs are expected to exhibit high corrosion resistance owing to their higher molybdenum content, which supports an increase in Cr_2O_3 layer thickness and a shorter repassivation time compared to medical-grade stainless steels such as 316L. The chemical composition, duplex microstructure, and surface properties of DSSs support their favorable corrosion performance. Stainless steels intended for use as implants are required to demonstrate

excellent corrosion resistance. Based on the results of the electrochemical corrosion tests in SBF (Table IV), the corrosion rates of the BM and laser-welded DSS were determined to be within the acceptable range for implant applications. The corrosion resistance of stainless steels can also be associated with surface roughness and wettability. Numerous studies in the literature indicate that increasing hydrophilicity and surface roughness can lead to a decrease in corrosion resistance.[59–63] In this regard, the fact that the corrosion resistance of sample A3 which has the highest surface roughness and the lowest contact angle is lower than that of the BM which has the lowest surface roughness and the highest contact angle is consistent with existing literature. However, the lower corrosion resistance of samples A1 and A2 compared to sample A3, despite their higher surface hydrophilicity and lower surface roughness, is attributed to the formation of a lower fraction of the austenite phase in the microstructure following the welding process.

Surface images of the base material (sample A) and laser-welded samples following electrochemical corrosion testing are shown in Figure 11. When comparing the BM and WM, SEM images reveal that the WM surface exhibits more numerous and larger corrosion pits, with pits of varying morphologies observed on each sample surface. The BM exhibits this specific pit distribution and morphology owing to its balanced ferrite–austenite microstructure. The SEM images presented here provide further evidence of the superior corrosion resistance of the BM compared to the welded samples.

E. *Contact Angle and Surface Free Energy (SFE) Measurements*

Despite their high corrosion resistance, stainless steels are considered engineering materials with varying wettability.[64] Surfaces with a contact angle of less than 90 deg are described as hydrophilic, those between 90 and 150 deg as hydrophobic, and those greater than 150 deg as superhydrophobic.[65] The contact angles and SFE values of the DSS base material and laser-welded samples joined with different heat inputs were measured, and the results are presented in Figure 12. The findings of the study indicated a positive correlation between contact angle and SFE, whereby a reduced contact angle corresponded to a higher SFE value, whereas an increased contact angle corresponded to a lower SFE value. The BM (Sa = 1.05 μm) exhibited the highest

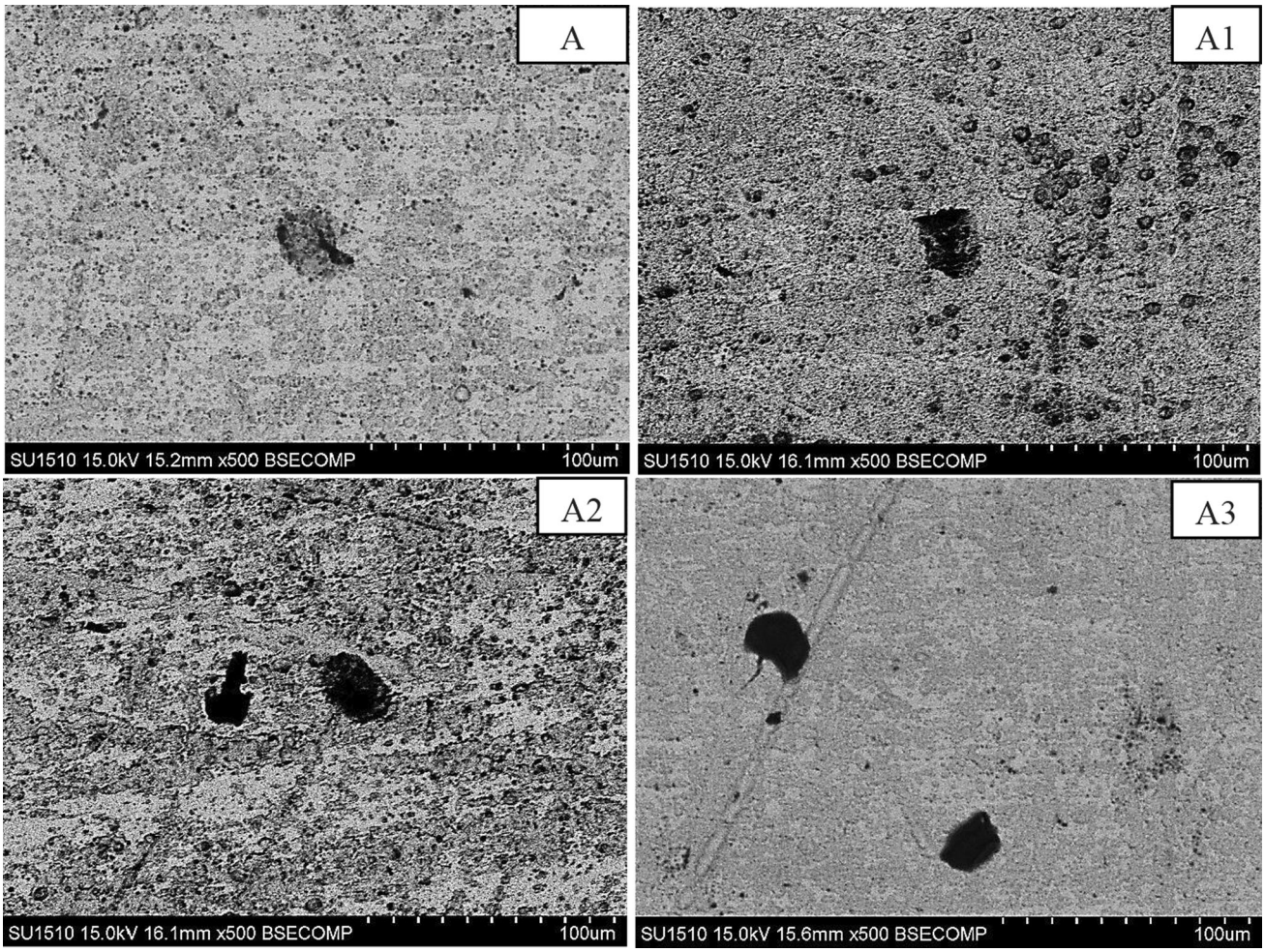

Fig. 11—Surface images of BM and laser-welded samples after electrochemical test.

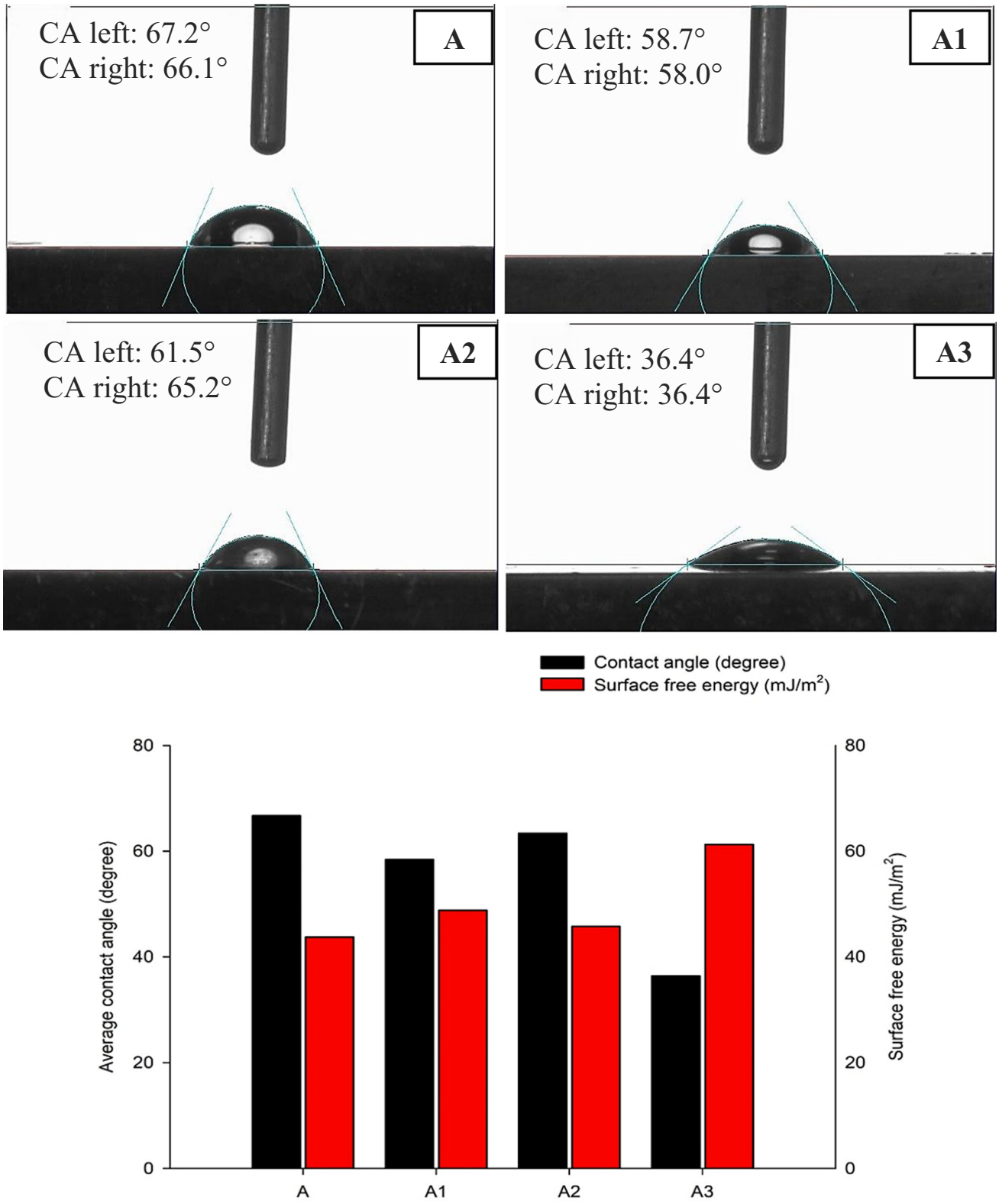

Fig. 12—Contact angle images and contact angles-SFE graphs of BM and laser-welded samples.

contact angle among the samples, while sample A3 (Sa = 2.97 μm) exhibited the lowest. It was noted that the contact angle of sample A1 (Sa = 1.39 μm) was higher than that of sample A2 (Sa = 1.07 μm). It was determined that both the BM and the laser-welded samples exhibited hydrophilic surfaces. The fact that the sample with the highest heat input had the lowest contact angle is attributed to its higher surface

roughness. Köse *et al*., who conducted a similar study, determined *via* atomic force microscopy (AFM) that the surface roughness of the weld bead increased as the welding heat input increased when DSS was joined by laser welding.[58] Researchers have also determined that an increase in the surface roughness of 316L stainless steel, used as an orthopedic implant material, causes a reduction in the contact angle.[66] Furthermore, it has been observed that the water contact angle decreases as the surface roughness of 316L stainless steel increases through nanosecond pulsed laser ablation.[67] Wenzel's theory explains the relationship between surface roughness and contact angle. According to this theory, increasing the roughness of a hydrophobic surface increases hydrophobicity, whereas increasing the roughness of a hydrophilic surface increases hydrophilicity.[68] The data obtained in this study indicate a negative correlation between surface roughness and contact angle, which is consistent with Wenzel's theory.

F. *Surface Topography*

Surface characterization of the BM and laser-welded samples was performed three-dimensionally using a surface profilometer (Figure 13). Areas of 250 μm × 250 μm were scanned from the weld center of the laser-welded A1, A2, and A3 samples, as well as from regions of the BM where the ferrite–austenite phase equilibrium exists. This enabled the quantitative evaluation of surface fluctuations on the micrometer scale. The obtained Sz, Sv, Sp, Sku, and Ssk values allow for a better understanding of the surface morphology. Sa (arithmetic mean height), Sq (root mean square height), Sz (maximum surface height), Sp (maximum peak height), Sv (maximum valley depth), Ssk (skewness), and Sku (kurtosis) are areal surface roughness parameters used to characterize the height distribution and morphology of the surface quantitatively. Although the same surface preparation procedures were applied to all samples prior to analysis, differences in surface roughness were observed. This difference is attributed to the heat input applied during the laser welding process.

An analysis of the surface roughness results (Table V) reveals significant differences among the samples. The lowest Sa value was observed for the BM sample at 1.05 μm, while the Sa value for the A3 sample, joined with higher heat input, was measured at 2.97 μm. Conversely, the Sa value of sample A2, joined with low heat input, was determined to be 1.07 μm. These results indicate that increasing the heat input leads to a substantial increase in surface roughness. When the Ssk and Sku values of sample A3 are examined, it is observed that the surface possesses a flatter geometry, with peak heights and valley depths becoming more pronounced. In contrast, in samples joined with low heat input, the surface morphology appears to consist of sharper, pointed structures, and the peak-to-valley difference is lower compared to the other samples. It is suggested that the increase in heat input facilitates the formation of distinct structures in the surface geometry by expanding the melt pool and prolonging the solidification time. The results obtained from samples joined with low heat input suggest that sharp structures are formed owing to the narrow melt pool and rapid solidification.[69,70] Previous studies have demonstrated that high heat input in laser welding induces a substantial increase in surface roughness.[58,71–74]

G. *In Vitro Cell Culture Assay*

Determining whether metallic implant materials cause toxic effects in the physiological environment of the body is of great importance. An additional MTT assay was applied to determine the presence of cytotoxicity. The cytotoxicity of the BM and laser-welded samples was evaluated using the hFOB cell line. For this purpose, sample extracts prepared by incubating the

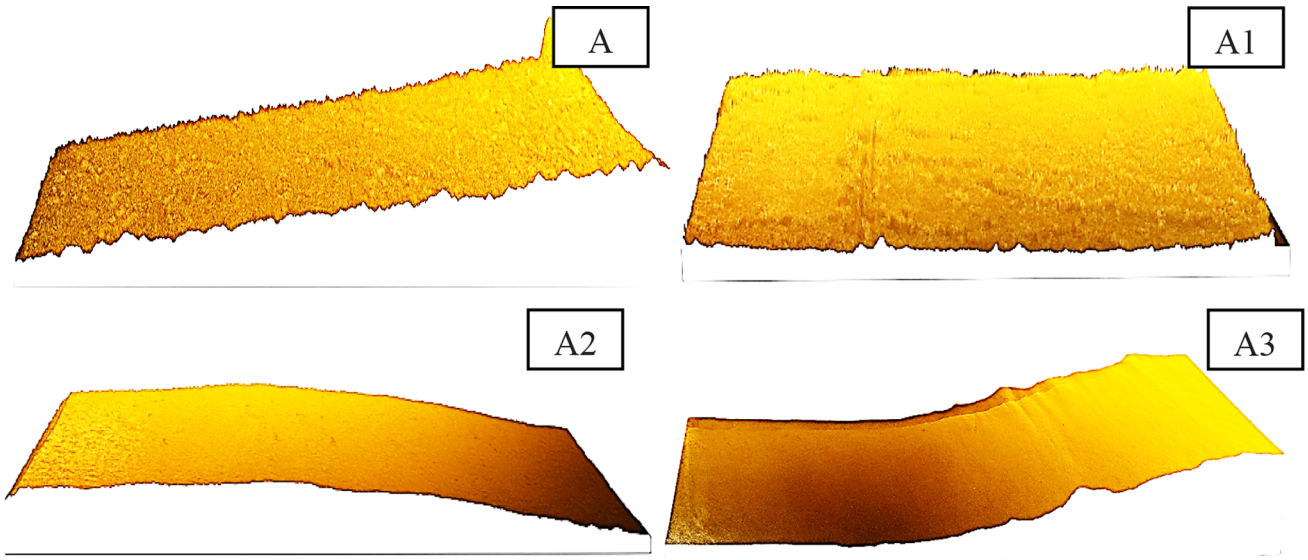

Fig. 13—3D surface topography of samples.

Table V. Parameters of Profilometer Surface Characterization

Samples	Sa (μm)	Sz (μm)	Sv (μm)	Sp (μm)	Sku	Ssk	Sq (μm)
A	1.05	7.95	3.29	4.65	2.35	− 0.0182	1.26
A1	1.39	7.18	3.31	3.87	1.86	0.0869	1.61
A2	1.07	5.87	3.45	2.42	2.84	− 0.606	1.34
A3	2.97	13.3	5.78	7.57	1.98	0.412	3.44

samples for 7, 14, 21, and 28 days in accordance with ISO standards were applied to healthy cells for 48 hours. The obtained results are shown in Figure 14. The cell viability ratios of all evaluated sample extracts were calculated by comparison with those of the negative control group. At the end of the incubation period, cell viability was above 70 pct, which is considered an acceptable threshold, for all incubation times in samples A, A1, A2, and A3. The viability values obtained from the 7-day extracts of samples A, A1, A2, and A3 were measured as 111, 105, 103, and 95 pct, respectively, compared to the control group. Cell viability exposed to the 28-day extracts was measured as 101, 106, 81, and 80 pct, respectively.

Although cell viability remained within acceptable limits for all groups and incubation periods, some differences between the groups were observed. In samples where the welding heat input increased, metal release decreased. The relatively lower cell viability observed in samples A2 and A3 compared to the other groups can be attributed to this reason. Metallic ions such as Mn, Ni, Mo, and Cr present in the environment at certain concentrations can support cell proliferation and growth and regulate cellular enzyme activity; however, concentrations above a specific threshold may cause toxicity.[64,75–77] Nevertheless, the results obtained in this study showed that samples with higher metallic ion

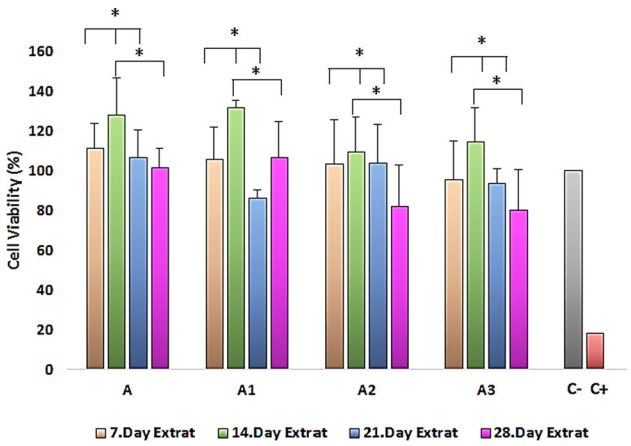

Fig. 14—Cell viability of Human Fetal Osteoblastic (hFOB) cells cultured with sample extracts at different incubation periods, measured by indirect MTT assay. Absorbance values were blank-corrected and normalized to the negative control group (set to 100 pct viability). Data are shown as mean ± SD ($n = 3$). Statistical significance was determined by pairwise two-tailed Student's t-tests ($^{*}P < 0.05$, $^{**}P < 0.01$, $^{***}P < 0.001$). Asterisks are annotated directly on the graph, with horizontal lines connecting the two groups being compared.

release and lower welding heat input exhibited higher cell viability than the others. Similarly, the ability of iron to participate in redox reactions makes it an important transition metal for cellular functions. However, the presence of excessive iron in the medium may also lead to DNA, protein, and membrane damage, which can reduce cell viability.[78] Therefore, the increasing iron release in the extract of sample A1 starting from day 14 may have relatively decreased cell viability. A similar trend was observed in the 28-day extract MTT results of sample A2. The decrease observed in the extract MTT results of sample A3 may be attributed to the fact that the amount of metallic ions required for healthy cellular metabolism is considerably lower in metals processed with higher heat input. When the overall cell viability results are considered, it can be concluded that the produced samples do not exhibit toxic effects on the cells and do not inhibit cell viability up to 28 days, depending on their ion release profiles. Researchers have associated reductions in cell viability with higher grain boundary (GB) energy and the presence of the ferrite phase in the weld microstructure. GBs possess higher energy, and the ferrite phase is an iron-rich phase. It has been reported that when ferrite grains are deficient in elements such as Cr, Ni, and/or Mo, which generally enhance corrosion resistance, this can result in a significant increase in the localized release of metallic ions into the surrounding cellular environment of the weld, thereby affecting cell viability.[23] When all results are evaluated, the high cell viability observed in some sample extracts, particularly in comparison with the negative control group, suggests that the controlled ion release profile of the produced samples is not only non-toxic but also cytocompatible. For osteoblastic cells (hFOB), the presence of transition metal ions such as Mn, Zn, and Mo at physiological trace levels is known to act as cofactors that upregulate enzymes essential for bone matrix mineralization and cell proliferation. Therefore, the sustained high viability is likely the result of a favorable balance between the beneficial effects of these trace elements and the prevention of cytotoxic accumulation, indicating a supportive environment for hFOB cell function rather than a detrimental one.[79,80] Metal ion toxicity on human osteoblast-like MG-63 osteosarcoma cells has been reported in the order Cr < Mg < Mo < Ni < Fe.[81] The lower cell viability observed in samples A1, A2, and A3 compared with sample A can be attributed to increased Fe release during the laser welding process. According to the inductively coupled plasma mass spectrometry (ICP-MS) results, the amounts of Cr, Ni, Mo, and Mn diffusing from the samples to the hFOB

cell line were at ppb levels, whereas the amount of Fe released was at ppm levels. Therefore, it was concluded that elements other than Fe were not released at concentrations that could induce cytotoxic effects.

Optical microscope images obtained after 24 hours of incubation show that the cells were fully spread and proliferated in each group and at each time point (Figures 15 and 16). The morphologically healthy structure of the cells indicates that the extracts did not cause any cytotoxic effects. The uniform spreading and homogeneous distribution of the cells suggest that they interacted harmoniously with the microenvironment. The MTT results also support these findings; the preservation of metabolic activity and high cell viability confirmed that the extracts did not have an adverse effect on cell viability. In addition, the maintenance of healthy cell morphology after 24 hours of incubation indicates that the extracts did not disrupt cell membrane integrity or induce cellular stress. The preservation of cell membrane integrity is generally achieved through the harmonious interaction of biocompatible materials and biological components with the cell surface.[66]

1. *The amount of elements diffusing into the human osteoblast cell environment from the experimental samples*

BM and laser-welded specimens were incubated in hFOB cell line medium, and the amounts of elements transferred from the samples to the cell medium on the 14th and 28th days of incubation were determined by the inductively coupled plasma mass spectrometry (ICP-MS) analysis (Table VI). The effect of welding heat input on the amounts of Cr, Mn, Fe, and Ni diffusing into the hFOB cell line medium on the 14th and 28th days of incubation for all examined samples was found to be statistically significant ($P < 0.05$). The difference between Mo release in samples A1 and A3 was found to be statistically insignificant ($P > 0.05$). It was determined that an increase in welding heat input caused a reduction in the release of Cr, Fe, Ni, and Mo. The highest element release occurred in the sample joined with the lowest welding heat input. The high element release observed in the sample joined with the lowest welding heat input is consistent with the higher corrosion rate of that sample. The diffusion mechanism can explain the release of metal ions from the samples. Metal release is related to the microstructure, surface properties, and surface quality of the weld area.[23,24,82] The pH and protein composition of the medium affect the amount of diffusing elements.[83] A decrease in pH

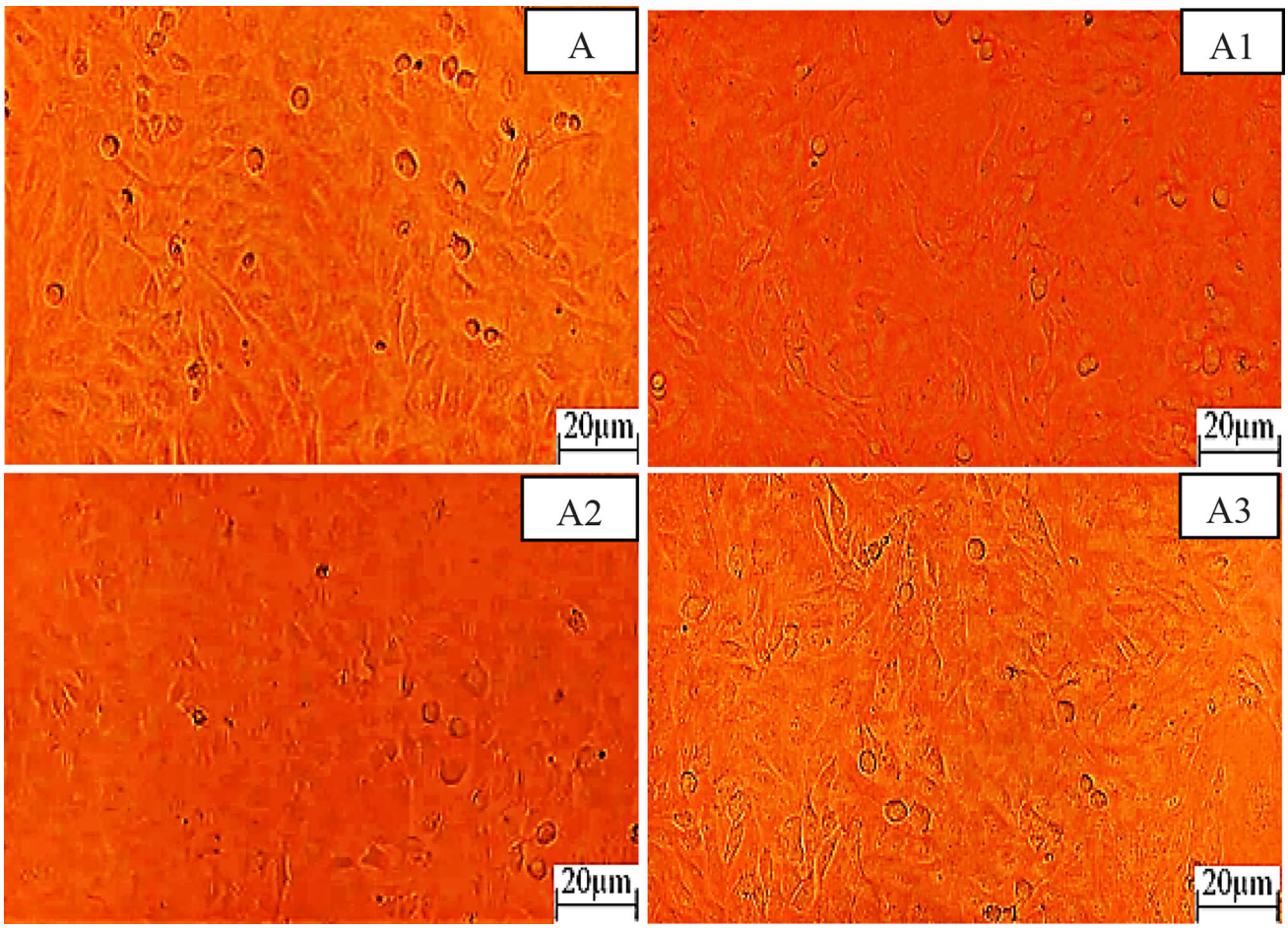

Fig. 15—Optical microscope images of the hFOB cell line on day 7 of incubation of A, A1, A2, and A3 samples.

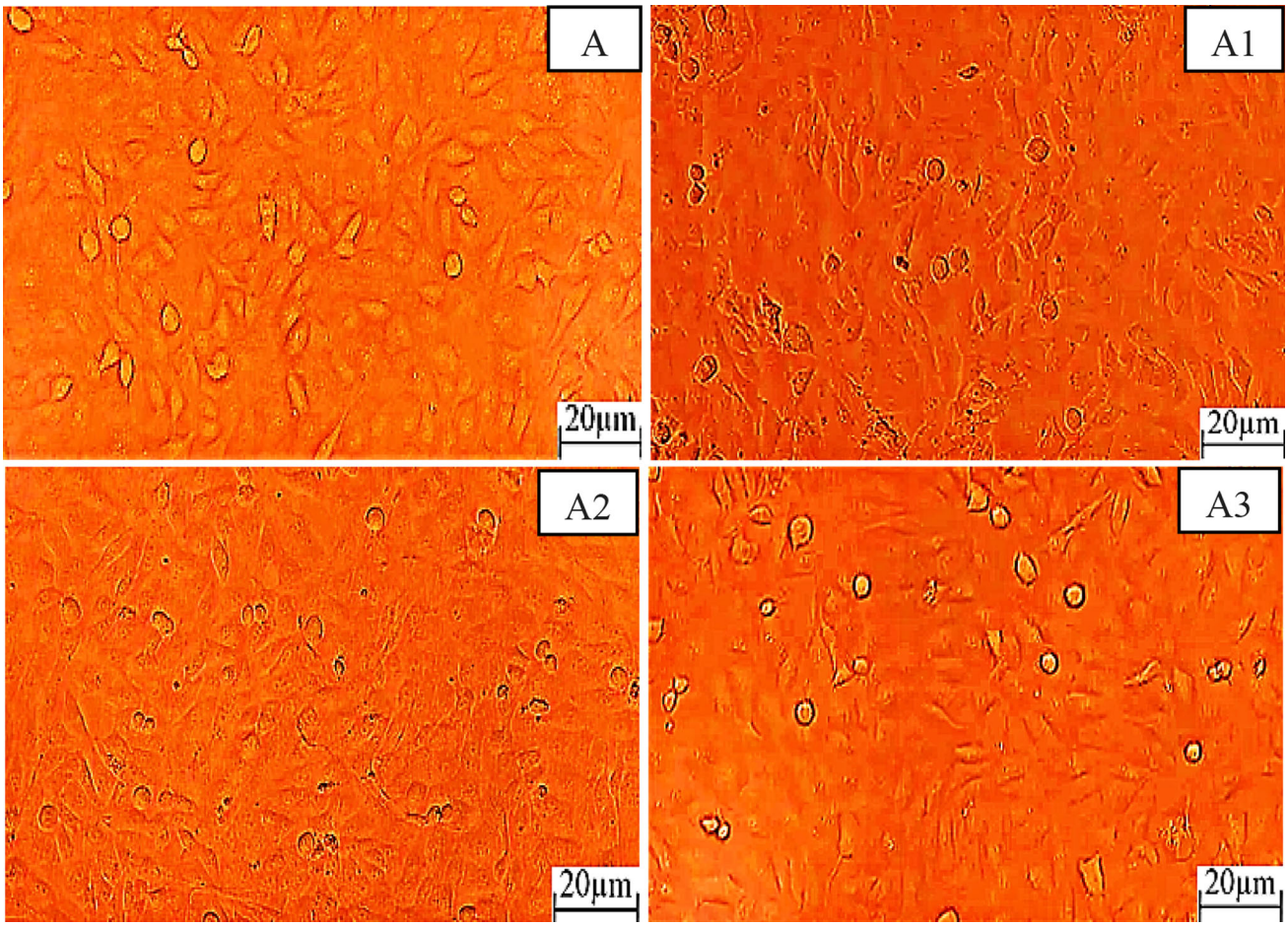

Fig. 16—Optical microscope images of the hFOB cell line on day 28 of incubation of A, A1, A2, and A3 samples.

Table VI. ICP-MS Results Obtained from the BM and Laser-Welded Samples After Different Incubation Times in the hFOB Cell Line Medium

Samples	Incubation Time	^{52}Cr (ng/mL)	^{55}Mn (ng/mL)	^{57}Fe (ng/mL)	^{60}Ni (ng/mL)	^{95}Mo (ng/mL)
A	14th day	$29.0^{C} \pm 2.0$	$5.5^{B} \pm 0.4$	$20.0^{D} \pm 70$	$18.0^{C} \pm 5$	$1.6^{B} \pm 1.2$
A	28th day	$77.02^{c} \pm 0.08$	$9.3^{c} \pm 0.6$	$665.0^{d} \pm 30$	$38.0^{c} \pm 2$	$2.4^{c} \pm 0.2$
A1	14th day	$22.18^{D} \pm 0.09$	$1.96^{C} \pm 0.04$	$742^{B} \pm 60$	$19.0^{C} \pm 2$	$1.7^{B} \pm 7$
A1	28th day	$266^{b} \pm 2.0$	$3.5^{b} \pm 0.7$	$1850^{b} \pm 80$	$193^{a} \pm 3$	$22^{b} \pm 2$
A2	14th day	$71.6^{A} \pm 0.9$	$14.6^{A} \pm 0.6$	$1374^{A} \pm 40$	$64.7^{A} \pm 1$	$10.1^{A} \pm 0.4$
A2	28th day	$275.0^{a} \pm 2$	$19.1^{a} \pm 0.2$	$2717^{a} \pm 10$	$95.2^{b} \pm 2$	$37.8^{a} \pm 1.3$
A3	14th day	59.7 ± 1.4	$0.8^{D} \pm 0.3$	$556^{C} \pm 30$	$22.7^{B} \pm 1.0$	$1.0^{B} \pm 0.9$
A3	28th day	63 ± 2.0	$8.86^{d} \pm 0.02$	$1256^{c} \pm 60$	$36.4^{c} \pm 0.5$	$22.1^{b} \pm 1.2$
LOD		0.0179	0.0075	1.6539	0.0112	0.0386
LOQ		0.0597	0.0250	5.5130	0.0373	0.1286

*Capital letters indicate the difference between welding heat inputs on element release up to day 14 of incubation, lowercase letters indicate the difference between welding heat inputs on element release up to day 28 of incubation ($P < 0.05$), $n = 3$, ± standard deviation.

induces the release of Mn, while the presence of proteins promotes the release of Fe, Ni, Cr, and Mn. However, the increase in metal release gradually decreases because the presence of proteins promotes Cr_2O_3 formation in the passive film structure formed on the surface.[84–88] The relatively high amount of element release observed within the short incubation period of 28 days is thought to be related to the thermal cycle of the weld. MTT test results indicate that the amount of metal ions released during the 28-day incubation period is not toxic to the cells. Since increasing the incubation time may decrease metal ion release due to the protein structure in the medium promoting Cr_2O_3 formation, implant applications are not expected to cause long-term cellular toxicity.

H. *Cell Attachment Assay*

The assessment of cell adhesion density in this assay was performed qualitatively through visual analysis of SEM images. To evaluate the extent to which the surface of the produced metallic samples supports cell attachment, hFOB cells were incubated on the sample surfaces for 48 hours following seeding. The fixed cells were subsequently analyzed using SEM. As shown in Figure 17, the hFOB cell line was observed to adhere to and proliferate on the surfaces of materials A, A1, A2, and A3. After 48 hours of incubation, the cells were observed to spread across the samples and cover the surfaces by extending their protrusions along the material. The adhesion and proliferation of the cells on the surface indicate a positive interaction between the metal samples and the cells. Moreover, the presence of cellular extensions suggests that the cells are capable of adhering to the sample surface, migrating across it, and potentially integrating with the material surface.[88] Visual examination revealed that cell adhesion was similar across all specimens, with no significant differences observed among them. Cell viability analyses further confirmed that the materials did not release any toxic substances that would inhibit cell proliferation, thereby supporting both cellular growth and adhesion.

I. *Bacterial Adhesion and SEM Images*

Biofilm layers formed by pathogenic microorganisms on implant materials and metallic medical equipment surfaces can cause serious infections and cross-contamination; furthermore, they are considered responsible for approximately 10 pct of biomaterial failures.[89] In stainless steel materials, the surface treatment method and surface isotropy are among the critical factors influencing bacterial attachment. Surface roughness, processing temperature, surface isotropy, and root mean square deviation all significantly affect bacterial adhesion. Researchers have particularly emphasized that increasing surface roughness leads to enhanced bacterial adhesion.[90,91] In the present study, bacterial adhesion to sample A3 (Sa = 2.97 μm), which possessed the highest Sa value, was determined to be 5 Log K_{ob}/mL/cm^2, whereas bacterial adhesion to the BM (Sa = 1.05 μm), which had the lowest Sa value, was measured at 4.6 Log K_{ob}/mL/cm^2. Researchers investigating the relationship between welding heat input and

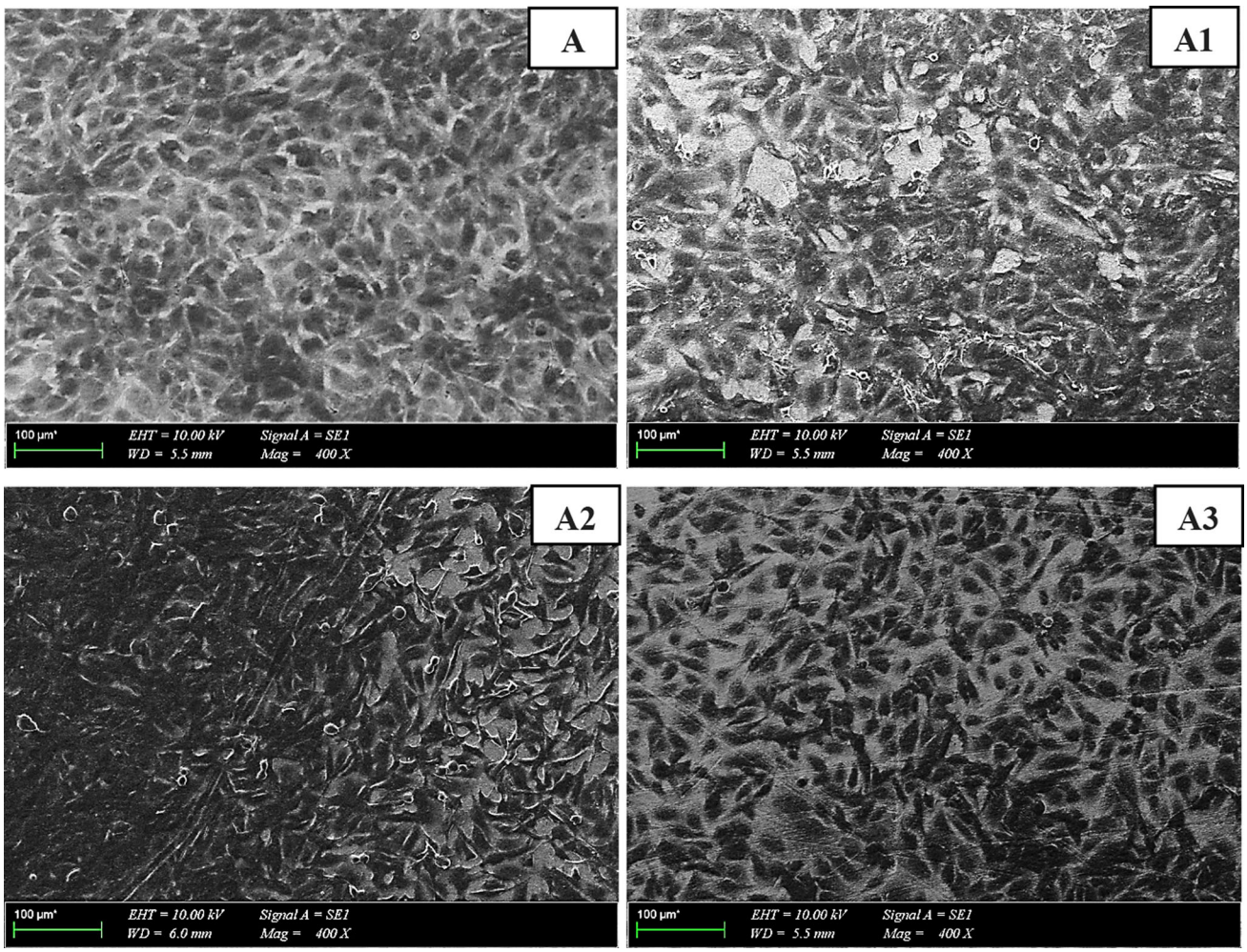

Fig. 17—SEM images of hFOB cell adhesion to BM and laser-welded samples.

bacterial adhesion measured the surface roughness values of AISI 304 austenitic stainless steel welded using metal inert gas (MIG) and tungsten inert gas (TIG) welding methods as 6.18 and 3.38 μm, respectively. They determined the total bacterial adhesion values to be 11,000 and 360 CFU/mL, respectively. Based on that study, it was observed that the weld seam obtained with lower welding heat input had a smoother structure and exhibited greater resistance to bacterial adhesion.[90] Results consistent with the aforementioned study were also obtained in the present research. The difference between the bacterial adhesion values of the DSS base material and samples welded with different welding heat inputs was found to be statistically significant ($P < 0.05$, Table VII). Notably, sample A3, which exhibited the highest bacterial adhesion, was the sample joined with the highest welding heat input. The elevated bacterial adhesion observed on sample A3 compared with the other samples is attributed to its higher surface roughness.

One of the most critical criteria affecting bacterial adhesion to stainless steel surfaces is the surface free energy (SFE). The Lifshitz–van der Waals interactions that occur during bacterial adhesion are significantly influenced by SFE. For a surface to resist bacterial adhesion, the SFE value should ideally be within the range of 20 to 30 mN/m,[88] as values outside this range tend to promote bacterial attachment.[92–94] Consistent with the literature, higher bacterial adhesion was observed on metallic surfaces with higher SFE values.[95] The SFE values of the samples followed the order A3 > A1 > A2 > A. The high bacterial adhesion observed in sample A3, which possessed the highest SFE value, is in agreement with existing studies. Additionally, the BM, which had the lowest SFE value, exhibited greater resistance to bacterial adhesion, supporting the notion that an increase in SFE promotes bacterial attachment. Another factor influencing bacterial adhesion is surface hydrophilicity. An increase in surface hydrophobicity reduces bacterial adhesion strength below the Laplace pressure, making attachment more difficult. Furthermore, bacterial adhesion to hydrophobic surfaces is hindered by the formation of air bubbles between the bacteria and the surface, as well as the reduction of van der Waals attraction between the bacteria and the substrate.[96] It has also been reported that an increase in surface hydrophilicity on stainless steel surfaces promotes bacterial adhesion.[97] The contact angle values of the surfaces examined in this study ranged from 37.4 to 67.2 deg, indicating that all surfaces were hydrophilic. It was observed that the laser welding process increased surface hydrophilicity, thereby promoting bacterial adhesion. The Cr and Mo contents in the chemical composition of stainless steels influence bacterial adhesion by affecting the thickness and stability of the passive film formed on the surface.[15,98] It has also been reported that high Ni content promotes bacterial adhesion.[63,99] EDS analysis showed that laser welding did not cause a substantial difference in the proportions of Cr, Ni, and Mo on the material surface. The similarity in the chemical compositions of the BM and laser-welded samples suggests that the bacterial adhesion observed in the samples is primarily influenced by physical parameters such as SFE, contact angle, and surface roughness rather than surface chemistry.

Table VII. Results of *E. coli* O157:H7 Adhesion Test on BM and Laser-Welded Samples (Log K_{ob}/mL/cm^2)

Sample	*E. coli* O157:H7
A	$4.6^{d} \pm 0.1$
A1	$4.9^{b} \pm 0.4$
A2	$4.7^{c} \pm 0.2$
A3	$5.0^{a} \pm 0.2$

*Letters indicate the difference between welding heat inputs, $n = 4$, ± standard deviation.

In their study, Casarin *et al*. investigated the adhesion of *Salmonella enteritidis* on the weld seam of 304L stainless steel joined by MIG and TIG welding.[100] The images obtained demonstrated that *S. enteritidis* tended to form clusters on the metal surface.[100] In another study, researchers examined the adhesion of *Listeria monocytogenes* to the surface of 304L stainless steel following 24 hours of incubation.[101] The images obtained after the incubation period showed that the bacteria tended to form colonies.[100,101] Within the scope of the present study, it was observed that *E. coli* O157:H7 adhered to the surfaces of the BM and laser-welded samples and exhibited a tendency to form colonies (Figure 18). It is well established that bacteria adhering to polished surfaces tend to form colonies.[100–102] Therefore, it is suggested that the polished surfaces of the materials used in this study facilitate such colony formation (Figure 18).

IV. CONCLUSIONS

The microstructure, microtexture, biocorrosion behavior, *in vitro* biocompatibility, and bacterial adhesion behavior of AISI 2205 DSS joined using various laser welding heat inputs were investigated. The main findings of this study are summarized as follows:

(1) The microstructure of the laser-welded DSS was predominantly composed of ferrite due to the rapid solidification associated with low welding heat input. While the BM exhibited a balanced ferrite–austenite structure, the welded samples showed a significantly higher ferrite fraction. No sigma phase, nitride, or carbide formations were detected.
(2) EDS, XRD, and EBSD analyses demonstrated that welding heat input had a limited effect on elemental distribution and phase composition. Only ferrite and austenite phases were identified, indicating that the laser welding process facilitates joining with minimal metallurgical degradation.
(3) Electrochemical corrosion tests in the SBF environment showed that the BM exhibited the highest E_{corr} and the lowest I_{corr} values. Among the welded specimens, sample A3 (joined with the highest welding heat input) demonstrated

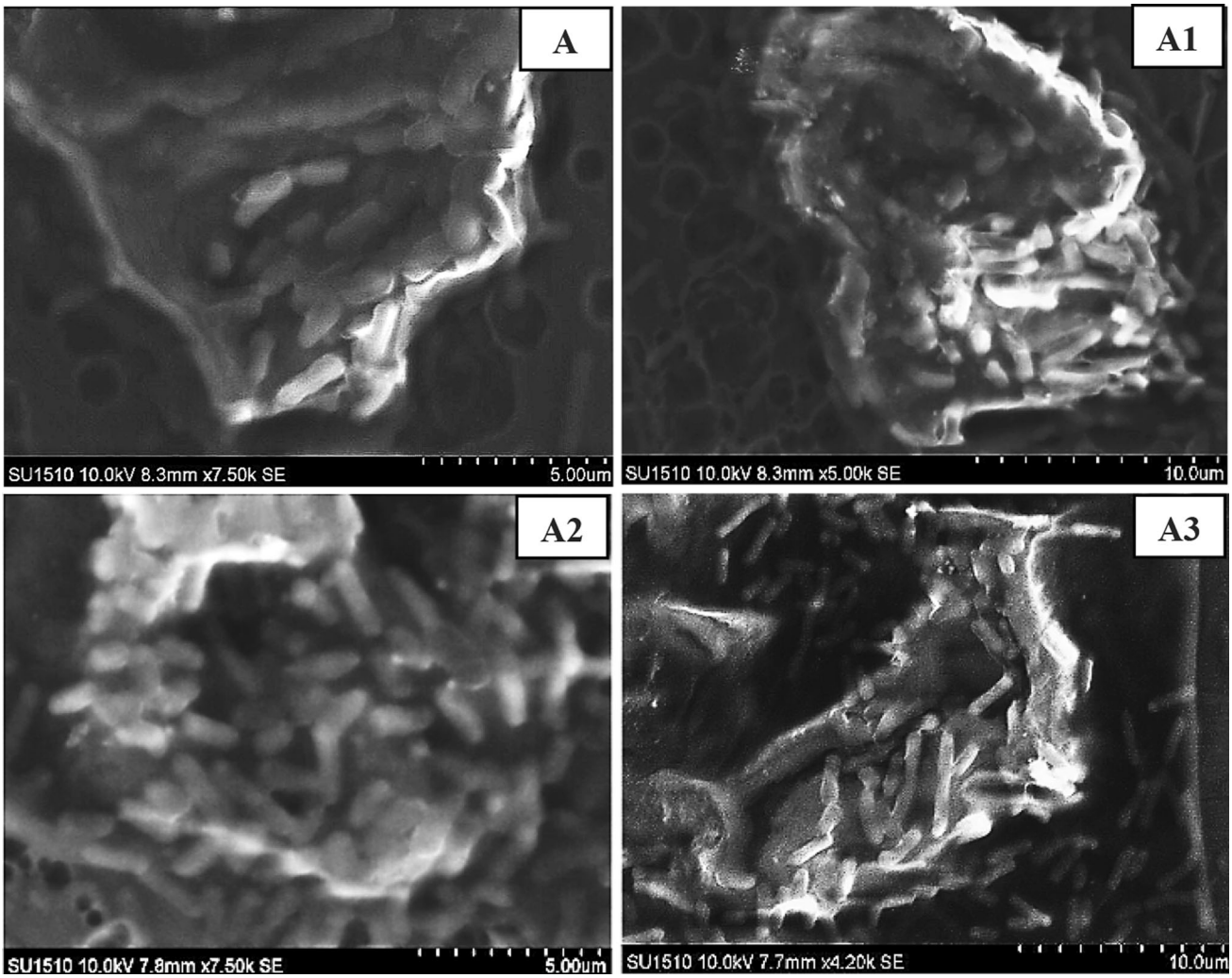

Fig. 18—SEM images of *E. coli* O157:H7 adhesion to BM and laser-welded samples.

relatively superior corrosion resistance, which is attributed to its higher austenite fraction, specific grain structure, and the presence of a [101] crystallographic orientation at the weld center.

(4) Surface characterization results indicated that laser welding increased surface roughness and hydrophilicity. Accordingly, the contact angle decreased with increasing welding heat input, with the lowest value observed in sample A3.

(5) MTT results demonstrated that neither the DSS base material nor the laser-welded samples exhibited cytotoxic effects on the hFOB cell line. Cell attachment behavior was similar across all samples, indicating that the laser welding process did not detrimentally affect cellular adhesion.

(6) The lowest bacterial adhesion was observed on the BM, whereas the highest adhesion occurred on sample A3, which possessed the highest welding heat input and surface roughness. SEM observations revealed that *E. coli* tended to form colonies on DSS surfaces. The results indicate that bacterial adhesion is primarily influenced by surface characteristics such as roughness, surface free energy, and wettability rather than metallurgical changes.

ACKNOWLEDGMENTS

The authors acknowledge use of characterization facilities within the David Cockayne Centre for Electron Microscopy, Department of Materials, University of Oxford, alongside financial support provided by the Henry Royce Institute (Grant ref EP/R010145/1).

AUTHOR CONTRIBUTIONS

Ceyhun Köse contributed toward conceptualization, methodology, original draft preparation, investigation, and writing—review & editing. Merve Gündüz contributed toward conceptualization, methodology, original draft preparation, investigation, and

writing—review & editing. Elif İlhan contributed toward conceptualization, methodology, original draft preparation, investigation, and writing—review & editing. Oğuzhan Gündüz contributed toward conceptualization, methodology, original draft preparation, investigation, and writing—review & editing. Salih Durdu contributed toward conceptualization, methodology, original draft preparation, investigation, and writing—review & editing. Segio Lozano-Perez contributed toward conceptualization, methodology, original draft preparation, investigation, and writing—review & editing.

DATA AVAILABILITY

Data will be made available on request.

CONFLICT OF INTEREST

The authors declare that they have no known competing financial interests or personal relationships that could have appeared to influence the work reported in this paper

FUNDING

Open access funding provided by the Scientific and Technological Research Council of Türkiye (TÜBİTAK).

OPEN ACCESS

This article is licensed under a Creative Commons Attribution 4.0 International License, which permits use, sharing, adaptation, distribution and reproduction in any medium or format, as long as you give appropriate credit to the original author(s) and the source, provide a link to the Creative Commons licence, and indicate if changes were made. The images or other third party material in this article are included in the article's Creative Commons licence, unless indicated otherwise in a credit line to the material. If material is not included in the article's Creative Commons licence and your intended use is not permitted by statutory regulation or exceeds the permitted use, you will need to obtain permission directly from the copyright holder. To view a copy of this licence, visit http://creativecommons.org/licenses/by/4.0/.

REFERENCES

1. L.E. Murr: *J. Mater. Sci. Technol.*, 2019, vol. 35(2), pp. 231–41. https://doi.org/10.1016/j.jmst.2018.09.003.
2. R.W. Gregorutti, J.E. Grau, F. Sives, and C.I. Elsner: *Mater. Sci. Technol.*, 2015, vol. 31(15), pp. 1818–24. https://doi.org/10.1179/1743284715Y.0000000017.
3. M. Sivakumar, U.K. Mudali, and S. Rajeswari: *J. Mater. Sci.*, 1993, vol. 28, pp. 6081–86.
4. Y. Zhang, S. Wu, and F. Cheng: *Mater. Sci. Eng. A*, 2022, vol. 854, p. 143809. https://doi.org/10.1016/j.msea.2022.143809.
5. H. He, Z. Liu, Y. Xie, L. Zhang, X. Yi, A. Fu, and W. Zhao: *Mater. Lett.*, 2024, vol. 360, p. 136003. https://doi.org/10.1016/j.matlet.2024.13600.
6. B.J. Tefft, S. Uthamaraj, J.J. Harburn, O. Hlinomaz, A. Lerman, D. Dragomir-Daescu, and G.S. Sandhu: *J. Magn. Magn. Mater.*, 2017, vol. 427, pp. 100–04. https://doi.org/10.1016/j.jmmm.2016.11.007.
7. A. Mahajan, S.S. Sidhu, and S. Devgan: *J. Phys. A*, 2020, vol. 126, p. 737. https://doi.org/10.1007/s00339-020-03940-5.
8. M.L. Gatto, G. Cerqueni, R. Groppo, E. Tognoli, A. Santoni, M. Cabibbo, et al.: *J. Funct. Biomater.*, 2023, vol. 14(10), p. 489. https://doi.org/10.3390/jfb14100489.
9. M.L. Gatto, A. Santoni, E. Santecchia, S. Spigarelli, F. Fiori, P. Mengucci, and M. Cabibbo: *Metals*, 2023, vol. 13(5), p. 949. https://doi.org/10.3390/met13050949.
10. Iu.H. Toor: *J. Mater. Eng. Perform.*, 2025. https://doi.org/10.1007/s11665-025-10781-x.
11. A. Pandey, A. Awasthi, and K.K. Saxena: *Adv. Mater. Process. Technol.*, 2020, vol. 6(2), pp. 405–40. https://doi.org/10.1080/2374068X.2020.1731236.
12. L. Peguet and A. Gaugain: *Metall. Res. Technol.*, 2011, vol. 108(4), pp. 231–43.
13. V. Muthupandi, P.B. Srinivasan, V. Shankar, S.K. Seshadri, and S. Sundaresan: *Mater. Lett.*, 2005, vol. 59(18), pp. 2305–09. https://doi.org/10.1016/j.matlet.2005.03.010.
14. Z. Xu, Y. Hou, M. Nele, G. Li, and S. Zhou: *J. Mater. Res. Technol.*, 2024, vol. 30, pp. 3474–84. https://doi.org/10.1016/j.jmrt.2024.04.082.
15. Y.T. Sun, X. Tan, L.L. Lei, J. Li, and Y.M. Jiang: *Tungsten*, 2021, vol. 3(3), pp. 329–37. https://doi.org/10.1007/s42864-021-00099-1.
16. D. Hwangbo, Y.R. Yoo, S.H. Choi, S.J. Choi, and Y.S. Kim: *Corros. Sci. Technol.*, 2022, vol. 21(4), pp. 273–81. https://doi.org/10.14773/cst.2022.21.4.273.
17. A. Kocijan, M. Conradi, and P.M. Schön: *J. Biomed. Mater. Res. B*, 2012, vol. 100B(3), pp. 799–807. https://doi.org/10.1002/jbm.b.32513.
18. A. Kocijan, D.K. Merl, and M. Jenko: *Corros. Sci.*, 2011, vol. 53(2), pp. 776–83. https://doi.org/10.1016/j.corsci.2010.11.010.
19. A.S. Hammood: *J. Appl. Biomater. Funct. Mater.*, 2020, vol. 18, p. 2280800019896215. https://doi.org/10.1177/2280800019896215.
20. A.S. Hammood, A.F. Noor, and M.T. Alkhafagy: *J. Mater. Sci. Mater. Med.*, 2017, vol. 28, p. 187. https://doi.org/10.1007/s10856-017-5997-1.
21. N.S. Al-Mamun, K.M. Deen, W. Haider, E. Asselin, and I. Shabib: *Addit. Manuf.*, 2020, vol. 34, p. 101237. https://doi.org/10.1016/j.addma.2020.101237.
22. A.S. Rajput, M. Das, and S. Kapil: *Proc. Inst. Mech. Eng. E*, 2022. https://doi.org/10.1177/09544089221107.
23. C. Köse, R. Kaçar, A.P. Zorba, M. Bağırova, and A.M. Allahverdiyev: *Mater. Sci. Eng. C*, 2016, vol. 60, pp. 211–18. https://doi.org/10.1016/j.msec.2015.11.035.
24. C. Köse, R. Kacar, A.P. Zorba, M. Bagırova, E.Ş Abamor, and A.M. Allahverdiyev: *Mater. Sci.*, 2018, vol. 24, pp. 159–65. https://doi.org/10.5755/j01.ms.24.2.18006.
25. T. Kokubo and H. Takadama: *Biomaterials*, 2006, vol. 27(15), pp. 2907–15. https://doi.org/10.1016/j.biomaterials.2006.01.017.
26. ISO: *ISO 10993–5:2009(E) 10993–5: Biological Evaluation of Medical Devices—Part 5: Tests for In Vitro Cytotoxicity*, 3rd edn, International Organisation of Standards, Geneva, 2009.
27. ISO: *ISO 10993-12 (1996) and ISO/DIS 10993-12 (2001) Biological Evaluation of Medical Devices—Part 12: Sample Preparation and Reference Materials*, ISO, Geneva.
28. V. Cannella, R. Altomare, V. Leonardi, L. Russotto, S. Di Bella, F. Mira, and A. Guercio: *BioMed Res. Int.*, 2020, vol. 2020, p. 8676343. https://doi.org/10.1155/2020/8676343.

29. Y. Zhai, W. Tian, K. Chen, L. Lan, J. Kan, and H. Shi: *Food Microbiol.*, 2024, vol. 117, p. 104383. https://doi.org/10.1016/j.fm.2023.104383.
30. T.V. Klug, J. Novello, D.C. Laranja, T.A. Aguirre, A. de Oliveira Rios, E.C. Tondo, R.P. dos Santos, and R.J. Bender: *Food Bioprocess Technol.*, 2017, vol. 10, pp. 275–83. https://doi.org/10.1007/s11947-016-1812-0.
31. J. Singh and A.S. Shahi: *Mater. Corros.*, 2021, vol. 72, pp. 1350–69. https://doi.org/10.1002/maco.202012201.
32. A.M. El-Batahgy, A.F. Khourshid, and T. Sharef: *Mater. Sci. Appl.*, 2011, vol. 2(10), p. 1443. https://doi.org/10.4236/msa.2011.210195.
33. H.S. Abdo, A.H. Seikh, J.A. Mohammed, and T. Uzzaman: *Metals*, 2021, vol. 11(8), p. 1206. https://doi.org/10.3390/met11081206.
34. G.R. Mohammed, M. Ishak, S.N. Aqida, and H.A. Abdulhadi: *Metals*, 2017, vol. 7(2), p. 39. https://doi.org/10.3390/met7020039.
35. C. Köse: *Eng. Fail. Anal.*, 2024, vol. 158, p. 108025. https://doi.org/10.1016/j.engfailanal.2024.108025.
36. B. Šimeková, M. Dománková, I. Kovaříková, P. Kovačócy, M. Martinkovič, M. Šimek, and L. Ciuła: *Metals*, 2024, vol. 14(10), p. 1184. https://doi.org/10.3390/met14101184.
37. H. Sieurin and R. Sandström: *Mater. Sci. Eng. A*, 2006, vol. 418(1–2), pp. 250–56. https://doi.org/10.1016/j.msea.2005.11.025.
38. A. Eghlimi, M. Shamanian, M. Eskandarian, A. Zabolian, and J.A. Szpunar: *Mater. Charact.*, 2015, vol. 106, pp. 208–17. https://doi.org/10.1016/j.matchar.2015.05.036.
39. R. Lai, Y. Cai, Y. Wu, F. Li, and X. Hua: *J. Mater. Process. Technol.*, 2016, vol. 231, pp. 397–405. https://doi.org/10.1016/j.jmatprotec.2016.01.016.
40. C. Gennari, M. Lago, B. Bögre, I. Meszaros, I. Calliari, and L. Pezzato: *Metals*, 2018, vol. 8(12), p. 1074. https://doi.org/10.3390/met8121074.
41. E.J. Da Cruz Junior, J. Gallego, A.G. Settimi, C. Gennari, A. Zambon, and V.A. Ventrella: *J. Mater. Eng. Perform.*, 2021, vol. 30, pp. 3024–32. https://doi.org/10.1007/s11665-021-05590-x.
42. G.S. Da Fonseca, L.O.R. Barbosa, E.A. Ferreira, C.R. Xavier, and J.A. De Castro: *Metals*, 2017, vol. 7(12), p. 538. https://doi.org/10.3390/met7120538.
43. C. Köse: *Vacuum*, 2023, vol. 215, p. 112347. https://doi.org/10.1016/j.vacuum.2023.112347.
44. Y. Song, Q. Sun, K. Guo, X. Wang, J. Liu, and J. Sun: *Mater. Sci. Eng. A*, 2020. https://doi.org/10.1016/j.msea.2020.139879.
45. Y. Hong, C. Zhou, Y. Zheng, L. Zhang, and J. Zheng: *Mater. Sci. Eng. A*, 2021. https://doi.org/10.1016/j.msea.2020.140279.
46. C.T.J. Panicker and V. Senthilkumar, *Prog. Addit. Manuf.*https://doi.org/10.1007/s40964-025-01001-y.
47. A. Ask, S. Forest, B. Appolaire, K. Ammar, and O.U. Salman: *J. Mech. Phys. Solids*, 2018. https://doi.org/10.1016/j.jmps.2018.03.006.
48. Z. Che, H. Xue, J. Liu, X. Zhou, W. Liu, S. Yang, Y. Du, X. Cheng, X. Li, and C. Liu: *Corros. Sci.*, 2025, vol. 248, p. 112810. https://doi.org/10.1016/j.corsci.2025.112810.
49. G. Song, A. Atrens, and M. Dargusch: *Corros. Sci.*, 1998, vol. 41(2), pp. 249–73. https://doi.org/10.1016/S0010-938X(98)00121-8.
50. Z. Shi, Z. Zhou, P. Shum, and L.K.Y. Li: *Appl. Surf. Sci.*, 2019, vol. 477, pp. 166–71. https://doi.org/10.1016/j.apsusc.2017.11.041.
51. H.S. Abdo, A.H. Seikh, U. Abdus Samad, A. Fouly, and J.A. Mohammed: *Crystals*, 2021, vol. 11(9), p. 1025. https://doi.org/10.3390/cryst11091025.
52. Z. Brytan and J. Niagaj: *Appl. Surf. Sci.*, 2016, vol. 388, pp. 160–68. https://doi.org/10.1016/j.apsusc.2016.01.260.
53. T. Chehuan, V. Dreilich, K.S. de Assis, F.V. de Sousa, and O.R. Mattos: *Corros. Sci.*, 2014, vol. 86, pp. 268–74. https://doi.org/10.1016/j.corsci.2014.06.004.
54. G. Ge, J. Hu, Y. Huo, Y. Liu, S. Tang, J. Ding, K. Zhang, and J. Li: *J. Solid State Electrochem.*, 2024, vol. 28(7), pp. 2125–38. https://doi.org/10.1007/s10008-023-05731-3.
55. S. Gudikandula and A. Sharma: *Metallogr. Microstruct. Anal.*, 2023, vol. 12, pp. 834–48. https://doi.org/10.1007/s13632-023-01001-w.
56. P. Wang, J. Zhao, L. Ma, X. Cheng, and X. Li: *Mater. Charact.*, 2021, vol. 179, p. 111385. https://doi.org/10.1016/j.matchar.2021.111385.
57. W. Li, X. Gao, X. Chen, H. Wang, C. Zhu, T. Li, et al.: *Anti-Corros. Methods Mater.*, 2025, vol. 72(3), pp. 431–43. https://doi.org/10.1108/ACMM-10-2024-3107.
58. C. Köse: *J. Mater. Sci.*, 2020. https://doi.org/10.1007/s10853-020-05326-7.
59. C. Ni, Y. Shi, and J. Liu: *Mater. Res. Express*, 2018, vol. 6(3), p. 036505. https://doi.org/10.1088/2053-1591/aaf2d3.
60. A.K. Singh, B.S. Kumar, P. Jha, A. Mahanti, K. Singh, V. Kain, and S. Sinha: *Appl. Phys. A*, 2018, vol. 124, pp. 1–9. https://doi.org/10.1007/s00339-018-2243-8.
61. P. Cisquini, S.V. Ramos, P.R.P. Viana, V.D.F.C. Lins, A.R. Franco Jr., and E.A. Vieira: *J. Mater. Res. Technol.*, 2019, vol. 8(2), pp. 1897–1906. https://doi.org/10.1016/j.jmrt.2019.01.006.
62. J. Li, L. Pan, Q. Fu, Y. Zhou, and N. Guo: *Surf. Coat. Technol.*, 2019, vol. 357, pp. 740–47. https://doi.org/10.1016/j.surfcoat.2018.10.050.
63. Y. Tang, N. Dai, J. Wu, Y. Jiang, and J. Li: *Materials*, 2019, vol. 12(5), p. 738. https://doi.org/10.3390/ma12050738.
64. Y. Shi, S. Cui, T. Zhu, S. Gu, and X. Shen: *J. Mater. Process. Technol.*, 2018, vol. 256, pp. 254–61. https://doi.org/10.1016/j.jmatprotec.2018.02.019.
65. S. Seçer, Su Geçirmeyen Akıllı Yüzeyler (31.07.2019). Tübitak Bilim Genç, 2019. https://bilimgenc.tubitak.gov.tr/makale/su-gecirmeyen-akilli-yuzeyler (07.10.2024, 19:40).
66. F. Biçer, S.M. Toker, M.N. Soykan, B. Türk Yılmaz, B. Yenice Gürsu, and O. Uysal: *ACS Omega*, 2024, vol. 9(42), pp. 43138–55. https://doi.org/10.1021/acsomega.4c07185.
67. J. Dong, Y. Liu, and M. Pacella: *Coatings*, 2024, vol. 14(4), p. 467. https://doi.org/10.3390/coatings14040467.
68. R.N. Wenzel: *Ind. Eng. Chem.*, 1936, vol. 28, pp. 988–94.
69. X. Meng, W. Wang, Y. Xie, N. Wang, X. Ma, J. Dong, et al.: *Mater. Charact.*, 2026, vol. 231, p. 115884. https://doi.org/10.1016/j.matchar.2025.115884.
70. W. Wang, Q. Chen, C. Zhou, Z. Li, N. Wang, Z. Weng, et al.: *J. Mater. Res. Technol.*, 2025. https://doi.org/10.1016/j.jmrt.2025.12.182.
71. J. Peng, S. Xie, T. Chen, X. Wang, X. Yu, L. Yang, Z. Ni, Z. Ling, Z. Yuan, J. Shi, and Z. Yang: *Crystals*, 2025, vol. 15(1), p. 35. https://doi.org/10.3390/cryst15010035.
72. J. Peng, S. Xie, Y. Tian, X. Wang, X. Yu, N. Chen, et al.: *Opt. Laser Technol.*, 2026, vol. 193, p. 114240. https://doi.org/10.1016/j.optlastec.2025.114240.
73. J. Yuan, L. Wang, C. Wang, G. Dong, J. Wang, Y. Li, et al.: *Arch. Civ. Mech. Eng.*, 2025, vol. 25(5), p. 277. https://doi.org/10.1007/s43452-025-01333-0.
74. C. Köse: *Int. J. Electrochem. Sci.*, 2016, vol. 11(5), pp. 3542–54.
75. S. Decker, E. Kunisch, A. Moghaddam, T. Renkawitz, and F. Westhauser: *J. Trace Elem. Med. Biol.*, 2021, vol. 68, p. 126827. https://doi.org/10.1016/j.jtemb.2021.126827.
76. X. Lü, X. Bao, Y. Huang, Y. Qu, H. Lu, and Z. Lu: *Biomaterials*, 2009, vol. 30(2), pp. 141–48. https://doi.org/10.1016/j.biomaterials.2008.09.011.
77. S. Prasadh, M. Gupta, and R. Wong: *Sci. Rep.*, 2022, vol. 12(1), p. 8259. https://doi.org/10.1038/s41598-022-12490-0.
78. C.H. Weiss, C. Merkel, and A. Zimmer: *Biotechnol. Prog.*, 2021, vol. 37(4), p. e3148. https://doi.org/10.1002/btpr.3148.
79. G. Taskozhina, G. Batyrova, G. Umarova, Z. Issanguzhina, and N. Kereyeva: *J. Clin. Med.*, 2024, vol. 13, p. 4679. https://doi.org/10.3390/jcm13164679.
80. K. Yusa, O. Yamamoto, M. Iino, H. Takano, M. Fukuda, Z. Qiao, and T. Sugiyama: *Arch. Oral Biol.*, 2016, vol. 71, pp. 162–69. https://doi.org/10.1016/j.archoralbio.2016.07.010.
81. N.J. Hallab, C. Vermes, C. Messina, K.A. Roebuck, T.T. Glant, and J.J. Jacobs: *J. Biomed. Mater. Res.*, 2002, vol. 60(3), pp. 420–33. https://doi.org/10.1002/jbm.10106.
82. B.D. Ratner, A.S. Hoffman, F.J. Schoen, and J.E. Lemons: *Biomaterials Science: An Introduction to Materials*, 3rd ed. Academic, New York, 2013.
83. M. Lundin, Y. Hedberg, T. Jiang, G. Herting, X. Wang, E. Thormann, et al.: *J. Colloid Interface Sci.*, 2012, vol. 366(1), pp. 155–64. https://doi.org/10.1016/j.jcis.2011.09.068.

84. Y. Hedberg, X. Wang, J. Hedberg, M. Lundin, E. Blomberg, and I. Odnevall Wallinder: *J. Mater. Sci. Mater. Med.*, 2013, vol. 24, pp. 1015–33. https://doi.org/10.1007/s10856-013-4859-8.
85. T. Cui, X. Xu, D. Pan, J. Ma, Z. Lu, J. Chen, X. Liang, S. Lozano-Perez, and T. Shoji: *J. Nucl. Mater.*, 2022. https://doi.org/10.1016/j.jnucmat.2022.153741.
86. Z. Shen, D. Tweddle, H.B. Yu, G.Z. He, A. Varambhia, P. Karamched, F. Hofmann, A.J. Wilkinson, M.P. Moody, L.F. Zhang, and S. Lozano-Perez: *Acta Mater.*, 2020. https://doi.org/10.1016/j.actamat.2020.05.010.
87. X. Xu, D. Pan, Y. Zhen, F. Zhou, Z. Lu, T. Cui, J. Chen, S. Li, M. Zhang, S. Lozano-Perez, and H. Hänninen: *Corros. Sci.*, 2025, vol. 256, p. 113213.
88. J.G.S. Vacchi, W.S. de Carvalho, C.P. Meinhardt, L.A. Bergmann, S.T. Amancio-Filho, and C.A.D. Rovere: *Surf. Interfaces*, 2025, vol. 71, p. 106882. https://doi.org/10.1016/j.surfin.2025.106882.
89. E. Ilhan, S. Ulag, A. Sahin, B.K. Yilmaz, N. Ekren, O. Kilic, M. Sengor, D.M. Kalaskar, F.N. Oktar, and O. Gunduz: *J. Mech. Behav. Biomed. Mater.*, 2020, vol. 114(November), p. 104219. https://doi.org/10.1016/j.jmbbm.2020.104219.
90. A.P. Simon, B.L. da Silva, E.F. Belusso, T.S. Mazzucatto, J.S. Santos, T. Trivinho-Strixino, and M.S. Sikora: *Surf. Coat. Technol.*, 2023, vol. 474, p. 130077. https://doi.org/10.1016/j.surfcoat.2023.130077.
91. S. Durdu, G. Cihan, E. Yalcin, K. Çavuşoğlu, A. Altinok, H. Sagcan, İ Yurtsever, and M. Usta: *Sci. Rep.*, 2023, vol. 13, p. 11423. https://doi.org/10.1038/s41598-023-38733-2.
92. J. Das, J.A. Chase, M.L. Partyka, E.R. Atwill, and B. Linke: *J. Food Prot.*, 2020, vol. 83(3), pp. 426–33. https://doi.org/10.4315/0362-028X.JFP-19-279.
93. Q. Zhao: *Surf. Coat. Technol.*, 2004, vol. 185(2–3), pp. 199–204. https://doi.org/10.1016/j.surfcoat.2003.12.009.
94. R.E. Baier, V.A. DePalma, and W.A. Dale: *Management of Occlusive Arterial Disease*, Yearbook Medical, Chicago, 1971, p. 147.
95. F. Alam and K. Balani: *J. Mech. Behav. Biomed. Mater.*, 2017, vol. 65, pp. 872–80. https://doi.org/10.1016/j.jmbbm.2016.10.009.
96. M. Mu, S. Liu, W. DeFlorio, L. Hao, X. Wang, K.S. Salazar, et al.: *Langmuir*, 2023, vol. 39(15), pp. 5426–39. https://doi.org/10.1021/acs.langmuir.3c00091.
97. N. Wurzler, G. Hidde, M. Schenderlein, and O. Ozcan: *Eng. Rep.*, 2022, vol. 4(1), p. e12458. https://doi.org/10.1002/eng2.12458.
98. H.Y. Tang, C. Yang, T. Ueki, C.C. Pittman, D. Xu, T.L. Woodard, et al.: *ISME J.*, 2021, vol. 15(10), pp. 3084–93. https://doi.org/10.1038/s41396-021-00990-2.
99. Y. Bertan and E. Yılmaz: *Trans. Indian Inst. Met.*, 2024. https://doi.org/10.1007/s12666-024-03287-y.
100. L.S. Casarin, A. Brandelli, F. de Oliveira Casarin, P.A. Soave, C.H. Wanke, and E.C. Tondo: *Int. J. Food Microbiol.*, 2014, vol. 191, pp. 103–08. https://doi.org/10.1016/j.ijfoodmicro.2014.09.003.
101. M.I. Hossain, M.F.R. Mizan, M. Ashrafudoulla, S. Nahar, H.J. Joo, I.K. Jahid, S.H. Park, K.K. Kim, and S.D. Ha: *Food Sci. Technol.*, 2020, vol. 118, p. 108864. https://doi.org/10.1016/j.lwt.2019.108864.
102. S. Wu, S. Altenried, A. Zogg, F. Zuber, K. Maniura-Weber, and Q. Ren: *ACS Omega*, 2018, vol. 3(6), pp. 6456–64. https://doi.org/10.1021/acsomega.8b00769.

Publisher's Note Springer Nature remains neutral with regard to jurisdictional claims in published maps and institutional affiliations.